Electronic Thesis and Dissertation Repository

7-26-2018 2:30 PM

Computational and Spectroscopic Studies in the Design of Tetrapyrrole Dyes for Dye-Sensitized Solar Cells

Angel (Qi Wen) Zhang
The University of Western Ontario

Supervisor
Stillman, Martin
The University of Western Ontario

Graduate Program in Chemistry

A thesis submitted in partial fulfillment of the requirements for the degree in Master of Science
© Angel (Qi Wen) Zhang 2018

Recommended Citation

Zhang, Angel (Qi Wen), "Computational and Spectroscopic Studies in the Design of Tetrapyrrole Dyes for Dye-Sensitized Solar Cells" (2018). *Electronic Thesis and Dissertation Repository*. 5446.
https://ir.lib.uwo.ca/etd/5446

www.manaraa.com

Abstract

Cyclic tetrapyrroles, like porphyrins, phthalocyanines, and chlorins, are of great interest for dye-sensitized solar cell (DSSC) applications due to their highly versatile structure, tunable π-based spectroscopic and electrochemical properties, and excellent stabilities. As well, they have a structural analogy with chlorophyll, a natural photosensitizer. Chlorophylls exhibit a red and intense lowest energy absorption band that is one of the ideal properties of a dye for application in DSSCs. However, because chlorophylls are unstable, it is necessary to design similar but more stable tetrapyrroles with these ideal properties. The relationship between chlorophyll's geometric structure and spectral properties were first explored using density functional theory (DFT) calculations. Understanding the unique electronic structure of the chlorophylls will help guide future designs of synthetic tetrapyrroles. The electronic structure of synthetic and fictive porphyrins and chlorins with β-substitutions were then probed using magnetic circular dichroism and DFT calculations.

Keywords

Chlorophyll, dye-sensitized solar cells, Grätzel cell, density functional theory, DFT, time dependent DFT, magnetic circular dichroism, MCD, porphyrins, chlorins, electronic structure, absorption, spectral properties, Q band, lumo, homo, Gouterman MOs

Co-Authorship Statement

This thesis contains material from previously published manuscripts. Dr. Martin Stillman is a co-author on all the published papers and was responsible for supervising and training Angel Zhang. For the chapters where a version was published, Angel Zhang wrote the first draft of the paper and Dr. Martin Stillman played a major role in the editing and revisions of the published manuscripts. Angel Zhang was responsible for acquiring all the data and preparing the figures.

For Chapter 4, Lydia Kwan carried out the preliminary spectral and computational analyses on the four synthetic porphyrins. Angel Zhang redid all the spectroscopic measurements and reworked all the data and computational analyses for the published paper.

The compounds in Chapter 4 and Chapter 5 were provided by Dr. Hong Wang and Dr. Franz-Peter Montforts, respectively. All spectroscopic measurements and computational analyses were carried out by Angel Zhang.

Acknowledgements

I am sincerely grateful to my close friends Daisy Sun and Debbie Chan for being there and helping me get through the beginning the part of my Masters studies.

My sincerest thanks to my supervisor and mentor, Dr. Martin Stillman, for the continuous support and guidance of my research and other matters. Thank you for taking the time to discuss my questions and concerns. All of your stories and "jokes" has made my stay enjoyable. I certainly will miss the wonderful people and atmosphere of lab. It was a pleasure working with everyone.

Special thanks to Daisy Wong for educating me on the histories of the places we visited together for conferences. You were an amazing personal tour guide and I really enjoyed spending time with you.

Thank you Dr. Zhifeng Ding for sharing with me your insights and helping me out on certain issues. Thank you Mr. John Vanstone and members of the Electronic Shop for keeping our instruments and computers running.

Table of Contents

v

List of Tables

List of Figures

List of Appendices

List of Abbreviations and Definitions

B band	Blue region absorption band for tetrapyrroles
BM	Bohr magneton
CAM-B3LYP	Coulomb-attenuated hybrid exchange-correlation functional
CB	Conduction band
Chl	Chlorophyll
DCM	Dichloromethane
DSSCs	Dye-sensitized solar cells
DFT	Density functional theory
ESOP	Excited state oxidation potential
GSOP	Ground state oxidation potential
H_2P	Free base porphyrin
H_2TPP	Free base tetraphenylporphyrin
HOMO	Highest occupied molecular orbital
ΔHOMO	Energy difference between HOMO and HOMO-1
LUMO	Lowest unoccupied molecular orbital
ΔLUMO	Energy difference between LUMO and LUMO+1
M_L	Angular momentum
MCD	Magnetic circular dichroism
Nc	Naphthalocyanine

NIR	Near infrared
Pc	Phthalocyanine
PCE	Power conversion efficiency
PCM	Polarizable Continuum Model
PM5	Parameterized model 5
Q band	Lowest energy absorption band for tetrapyrroles
S_0	Ground state
S_1	First excited state
S_2	Second excited state
TD-DFT	Time-dependent density functional theory
ZnP	Zinc porphyrin
ZnPc	Zinc phthalocyanine
ZnTPP	Zinc tetraphenylporphyrin

Chapter 1

1   Introduction

Tetrapyrroles are important compounds that play major and diverse roles in Nature. Notable functions include oxygen transport and storage (hemoglobin and myoglobin), photosynthesis (chlorophyll), electron transport (cytochromes), and catalysis (vitamin B12).[1] Their diverse roles are due to their highly versatile ring structure and ability to bind a variety of metals.[2] Tetrapyrroles are known in many subclasses, for example, porphyrins and chlorins in Nature, and phthalocyanines in the synthetic laboratory (Figure 1-1). Their optical spectra vary significantly in the blue and red regions of the visible spectrum. The remarkable chemical and photophysical properties of tetrapyrroles make them promising candidates for many applications including the dyes in dye-sensitized solar cells (DSSCs) and photodynamic therapy.[3-5] Strong absorption in the red to near infrared (NIR) region is necessary for high efficiency for both of these applications. This thesis will focus on the design of tetrapyrroles for DSSCs using the spectroscopic and theoretical data of chlorophyll as a starting point.

1.1   Structure and Nomenclature of Tetrapyrroles
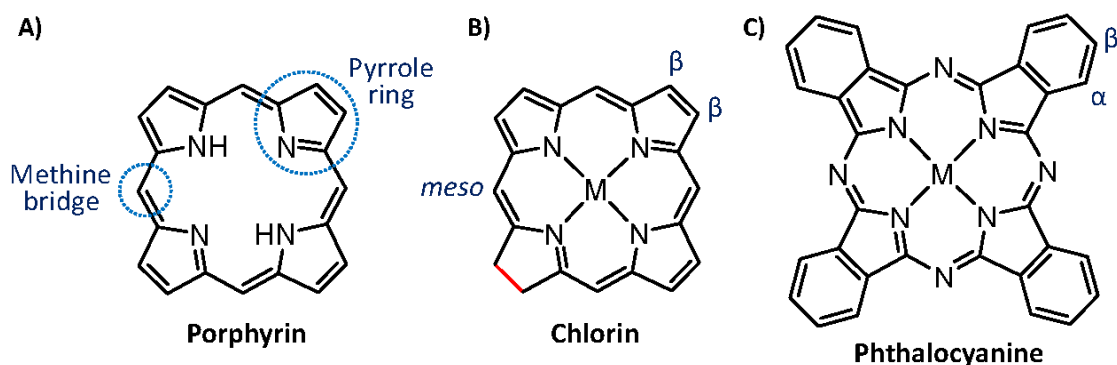
Figure 1-1 Structures of a free base porphyrin (A) and a metallated chlorin (B) and phthalocyanine (C). The pyrrole ring, methine bridge, α-, β-, and *meso*-positions are also labeled.

Tetrapyrroles are composed of four pyrrole rings linked together by methine (=CH–) bridges.[6] They have 18 π-electrons which satisfy Hückel's rules of 4n+2 for aromaticity (a principle quantum number of n=4). Fully unsaturated tetrapyrroles are called porphyrins (Figure 1-1A). A porphyrin without a metal ion is referred to as a free base (H_2P). Upon metallation, the two pyrrolic nitrogen atoms are deprotonated to form a dianionic porphyrin ring. The dianionic porphyrin ligand can bind to a variety of metals, typically divalent, including magnesium, iron, nickel, and zinc. Reduction of a double bond on one of the pyrrole rings produces a chlorin (Figure 1-1B), which is the central ring structure of chlorophyll. Phthalocyanines have a fused benzene ring on each pyrrole ring and the methine bridge carbon atoms are replaced with nitrogen atoms (Figure 1-1C). Only porphyrins and chlorins are discussed in this thesis.
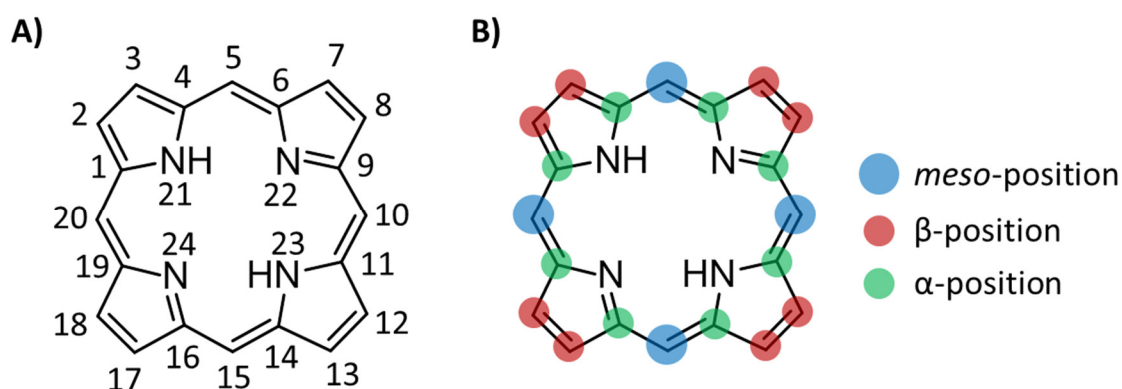
Figure 1-2 (A) IUPAC numbering system for porphyrins. (B) The more generic naming system of *meso*-, β-, and α-positions.

For nomenclature purposes, the carbon and nitrogen atoms in a porphyrin are numbered 1 – 24 (Figure 1-2A).[7] Figure 1-2B shows a more common naming system, where positions 5, 10, 15, and 20 are called '*meso*-positions', and positions 2, 3, 7, 8, 12, 13, 17, and 18, are referred to as 'β-positions'. As well, positions 1, 4, 6, 9, 11, 14, 16, and 19 are called 'α-positions'. The large number of positions that can be functionalized offer many possible molecular designs. Metallation, changes to the ring structure, and peripheral substituents influence the absorption and electronic properties of tetrapyrroles.

1.2 Absorption and Magnetic Circular Dichroism Spectra of Tetrapyrroles

Due to the highly conjugated π-system in tetrapyrroles, both natural and synthetic tetrapyrroles are deeply coloured. The slight changes to the ring structure between porphyrins, chlorins, and phthalocyanines (Pc) result in different spectral properties (Figure 1-3).[8] Although they all exhibit absorption in the blue (B band) and red (Q band) region, the relative intensities of these bands differ significantly. Magnetic circular dichroism (MCD) spectroscopy can be used to measure the change in electronic structure and underlying angular momentum of the tetrapyrroles that results in the different absorption properties.[9]
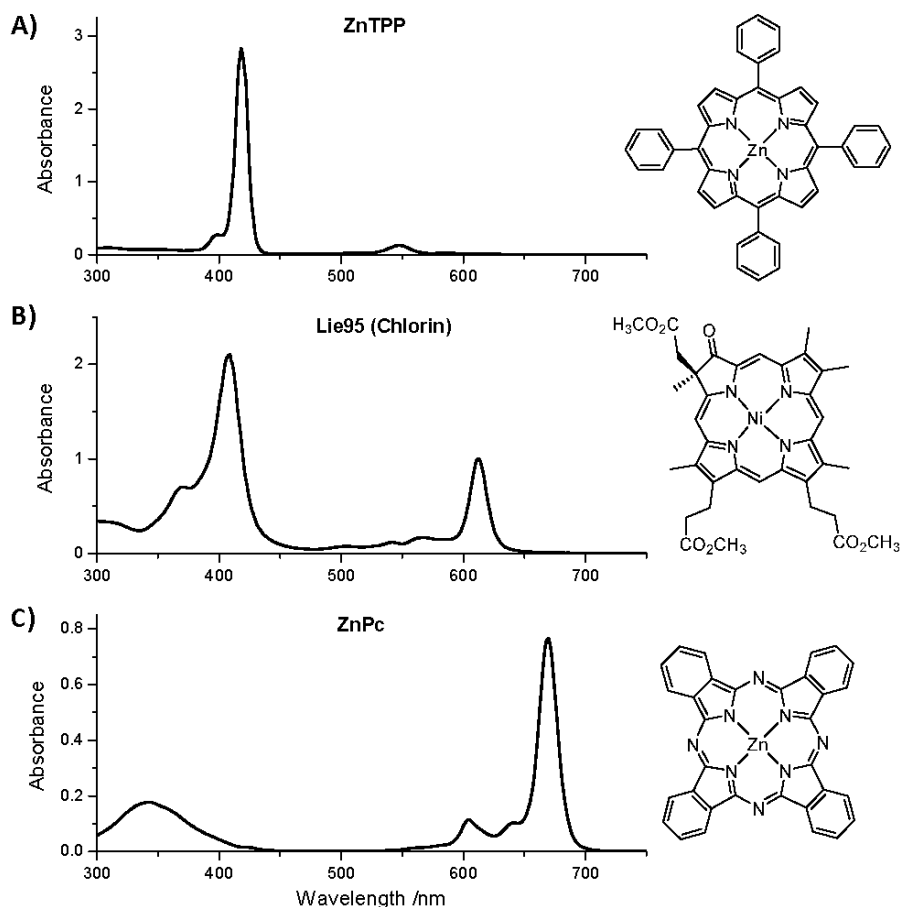
Figure 1-3 The absorption spectra of (A) ZnTPP, (B) a synthetic chlorin, Lie95[10], and (C) ZnPc. The absorption spectrum of **Lie95** resembles that of a simple methyl-substituted chlorin[11, 12] so it is used here as an example of a chlorin spectrum.

1.2.1   Origin of the Optical Spectra

In 1959, Gouterman proposed the four-orbital model to explain the absorption spectra of tetrapyrroles.[13] His model states that the absorption bands of porphyrins arise from transitions between two highest occupied molecular orbitals (HOMO, HOMO-1) and two lowest unoccupied molecular orbitals (LUMO, LUMO+1), Figure 1-4A.[14] These four orbitals can be referred to as Gouterman's MOs.[15] For metalloporphyrins of D_{4h} symmetry, the HOMO pair are of a_{1u} or a_{2u} symmetry character and can be accidentally degenerate while the LUMO pair have e_g character (e_{gx} or e_{gy}) and are usually doubly degenerate. In addition, the HOMO pair and LUMO pair have angular momenta (M_L) of ± 4 BM and ± 5 BM, respectively. The angular momentum of each orbital also corresponds to the number of nodes; the two HOMOs have 4 nodes and the two LUMOs have 5 nodes each. The occupied MO of a_{1u} character is identified with nodes that pass through the pyrrole nitrogen atoms and the occupied MO of a_{2u} character is identified with four nodes at 22.5^o from the a_{1u} nodes. The orientation of the nodal planes will be important when discussing the effect of substituent position on the energies of the Gouterman MOs.

Electronic transitions between the four Gouterman MOs give rise to two excited states, S_1 and S_2. Transitions from the ground state (S_0) to the first (S_1) and second (S_2) excited states gives rise to the observed Q and B band, respectively (Figure 1-4B). The S_1 and S_2 excited states are of E_u symmetry and they consist of a degenerate pair of states named S_{1x}, S_{1y} and S_{2x}, S_{2y}, respectively.[14] Transitions from the ground to the respective x and y states give rise to Q_x, Q_y, B_x, and B_y bands. The x and y subscripts denote the direction of polarization of the transition within the tetrapyrrole ring (the direction is reversed for chlorophyll with respect to porphyrins).[16, 17] Normally when there is not much splitting of the four MOs, the x and y components are degenerate and the absorption spectrum will show one Q band peak, with Q_x and Q_y superimposed on one another. The Q_x and Q_y bands are observed separately when the four MOs are split significantly. The B_x and B_y bands are split as well, but this is not as noticeable in the spectra. The energy difference between S_0 and S_1 is a more accurate relation to the energy of the Q band but the excited states are very complex as they are made of many transitions. Since the HOMO-LUMO transition is the major

contribution to the S_1 state, the HOMO-LUMO gap can be used to predict the energy of the Q band.
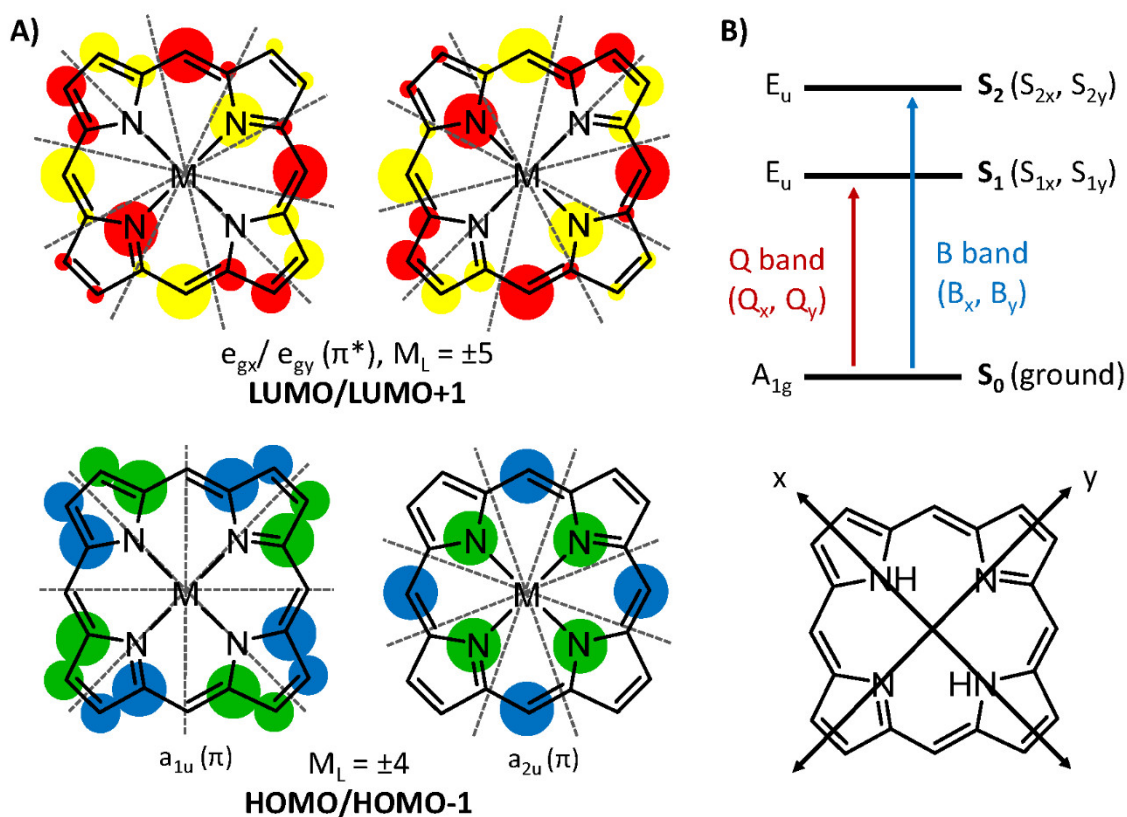
Figure 1-4 (A) Simplified electron density surfaces for the four Gouterman MOs. The blue and green shading represent the occupied π MOs, while the red and yellow shading represent the unoccupied π^* MOs. The nodes for the HOMO (4 nodes) and LUMO (5 nodes) are shown with grey dotted lines. **(B)** Origin of the Q and B bands (top) and the spectroscopic axis for porphyrins (bottom).

The absorption spectrum also exhibits vibronic bands that arise from transitions to the vibrational levels of the excited state. These vibronic bands appear at a lower wavelength (higher energy) than their respective absorption band. Vibronic bands are not shown in the theoretical spectra because the excited state vibrations are not included in the TD-DFT electronic state calculation.

The B and Q bands originate from allowed and forbidden transitions between the Gouterman MOs, respectively. Porphyrins typically have a nearly degenerate HOMO pair

and LUMO pair which leads to a weak forbidden Q band and an intense allowed B band. Splitting of the usually degenerate MOs, however, will break the selection rule that leads to the Q band being forbidden, and allows the borrowing of intensity from the allowed B band. The intensity of the Q and B bands are coupled so an increase in intensity of the Q band will lead to a decrease in the intensity of the B band. The reduction of the pyrrole in the chlorin macrocycle splits both the HOMO and LUMO pairs, which results in a more intense Q band, but slightly weaker B band (Figure 1-3). Of the three tetrapyrroles mentioned above, phthalocyanines exhibit the most intense Q band accompanied by two weak overlapping B bands.[18] The nitrogen atoms at the *meso*-positions selectively affects the a_{2u} MO of the HOMO pair more than the a_{1u} MO and introduces a significant energy split of over 2 eV.[19]

1.2.2   MCD Spectra Band Morphologies

MCD spectroscopy can identify subtle yet significant changes in the electronic structure to support the computational data of the underlying electronic structure.[9] This spectroscopic method has been used extensively to characterize and identify the origins of the electronic transition for symmetric tetrapyrroles, most notably for porphyrins and phthalocyanines.[8, 9] MCD signals arise from the difference in absorbance between left and right circularly polarized light, termed lcp and rcp, respectively. In the presence of a magnetic field, the excited states undergo Zeeman splitting. In Figure 1-5, it can be seen that lcp light interacts with $M_L = +1$ and rcp light interacts with $M_L = -1$.[20]
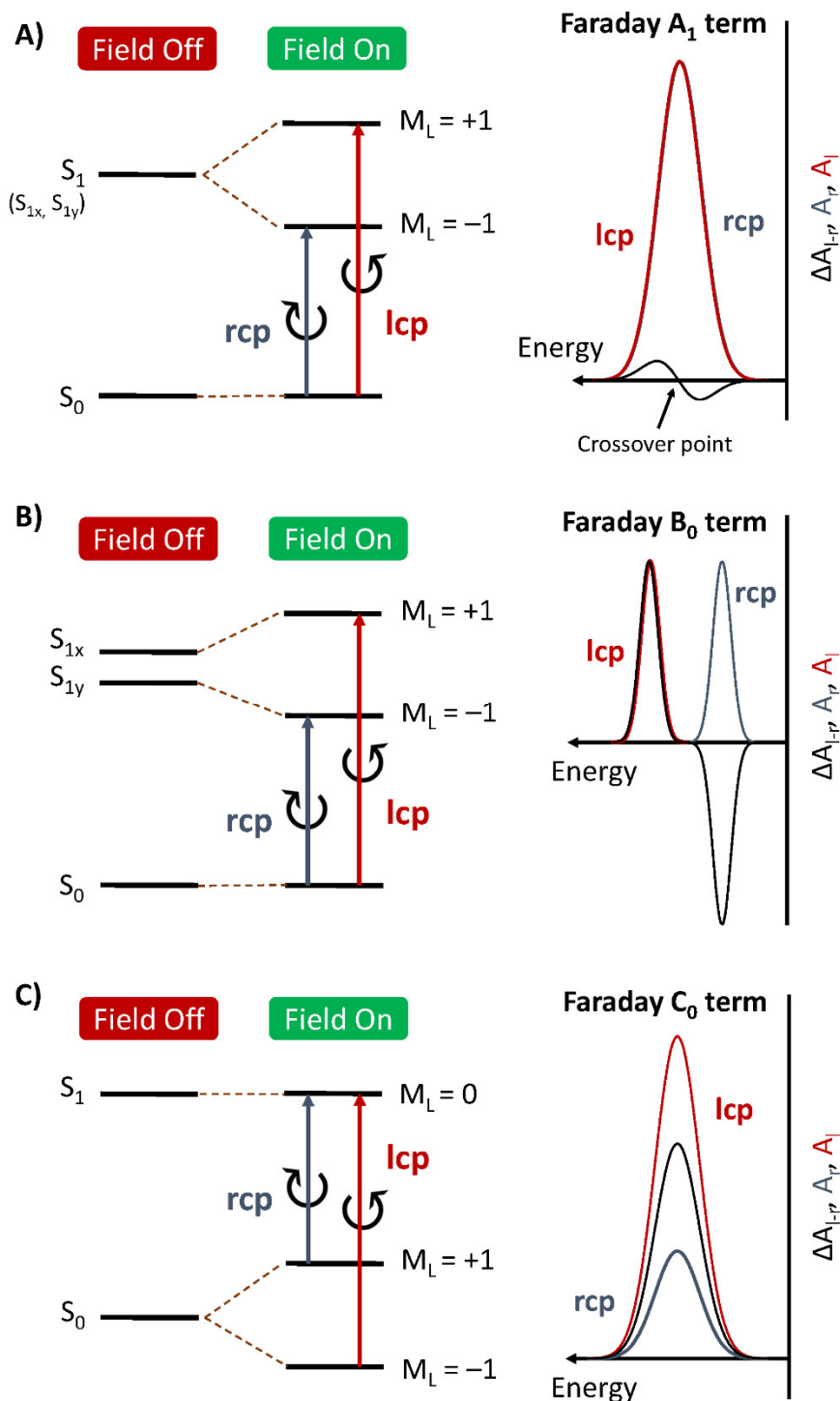
Figure 1-5 Origins of the Faraday A_1 term (A), B_0 term (B), and C_0 term (C). Splitting of the states are not to scale. The corresponding transition and band of lcp and rcp are shown in red and blue, respectively. The black band is the resultant of lcp minus rcp.

There are three Faraday terms in MCD spectroscopy that describes the observed band morphologies: A_1, B_0, and C_0. The appearance of these characteristic band shapes can be used to determine the degeneracies and relative angular momentum of the states (Figure 1-5). The A_1 term arises from the Zeeman splitting of degenerate excited states, for example, S_1 splitting into its x and y components under the presence of a magnetic field. The x and y components will have angular momenta of either +1 or -1. Because the magnetically induced split is relatively small, the resultant lcp (red) and rcp (blue) bands are almost completely overlapped. The difference between lcp and rcp produces a derivative shaped MCD signal (black) and the crossover point corresponds to the peak of the respective absorption band. The B_0 term arises from the Zeeman splitting of nondegenerate excited states. The energy difference between lcp and rcp will be relatively large compared with that of the A_1 term and the difference between lcp and rcp will give rise to a negative and a positive Gaussian shaped MCD signal. The energy separation of the lcp and rcp bands is proportional to the splitting of the positive and negative Gaussian shaped MCD signals (black line in Figure 1-5B). The peak of each B_0 term lines up with the associated absorption maximum. B_0 terms dominate the MCD spectra of molecules with low symmetry, where the ground or excited states are nondegenerate. The C_0 term arises from the Zeeman splitting of a degenerate ground state. It also has a Gaussian band shape, but can be distinguished from the B_0 term because it is temperature dependent.[21] The C_0 term is temperature sensitive since the ground states are populated based on the Boltzmann distribution.

Case A:

Case B:

Case C:
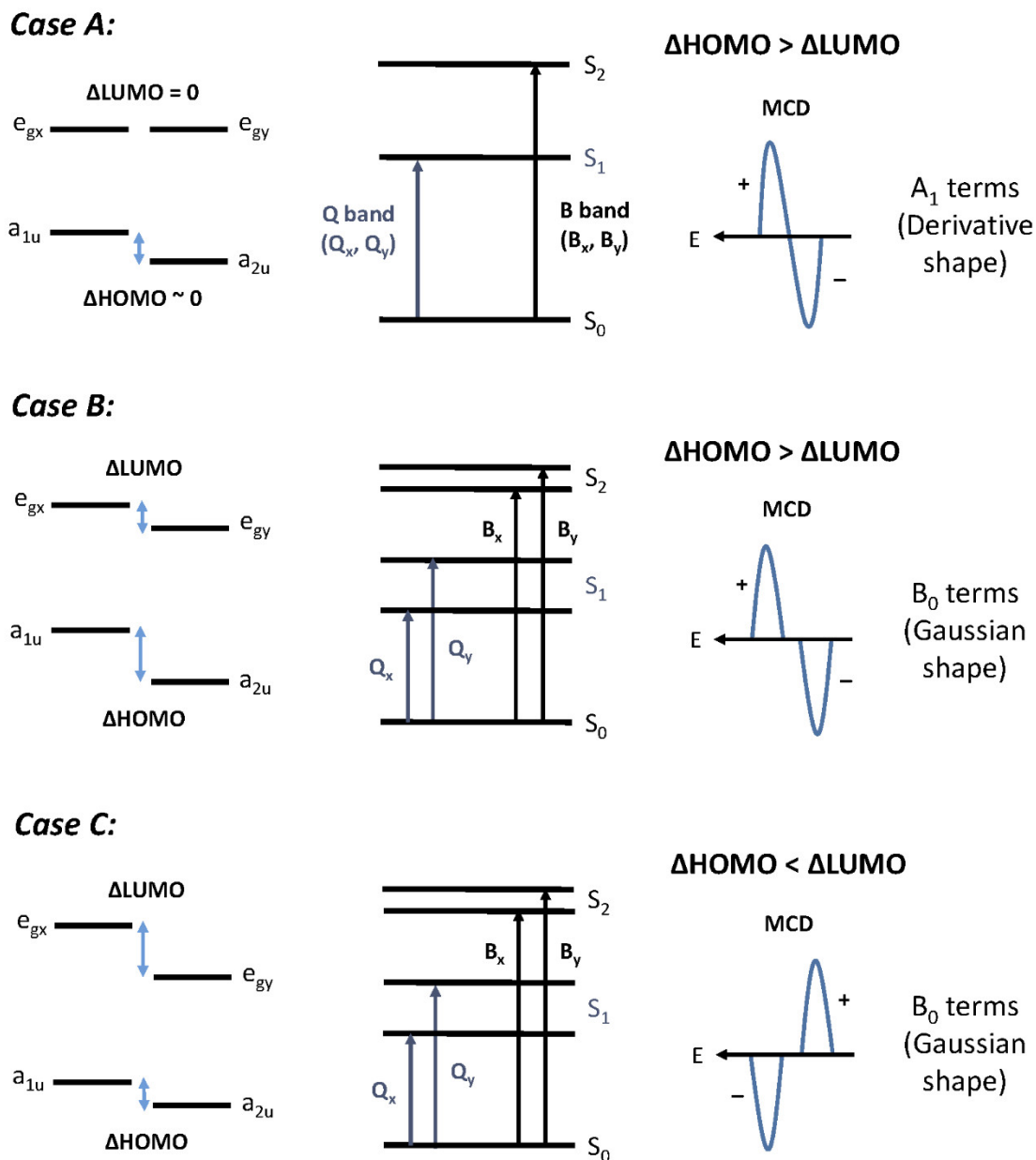
Figure 1-6 The three splitting patterns of the four Gouterman MOs and the resulting excited state degeneracies and MCD spectral morphologies. Energy splitting is not to scale.

There are three ways in which the HOMO pair and LUMO pair can split and each type of splitting results in a distinct MCD pattern (Figure 1-6).[22] The type of splitting depends on the nature of the substituents around the porphyrin ring core, the absence or presence of pyrrole ring reduction, and the symmetry of the overall molecule. Case A is normally

observed for tetrapyrroles with high symmetry. For these tetrapyrroles, the energy difference between the HOMO pair (ΔHOMO) may be nonzero, while the energy difference between the LUMO pair (ΔLUMO) is zero or close to zero. There will not be any splitting of the excited states and A_1 terms will be observed in the MCD spectrum. Lowering the symmetry of the molecule will result in either Case B or Case C, where the degeneracies of both the HOMO pair and LUMO pair are broken. The large splitting of the MOs results in the splitting of the excited states as well. This leads to the observation of B_0 terms in the MCD spectrum. When ΔHOMO is greater than ΔLUMO, a negative-to-positive MCD band pattern is observed in increasing energy (Case B). This is the normal situation for low symmetry tetrapyrroles. Certain geometric and electronic interactions between the peripheral substituents and the ring can split the LUMO pair significantly, such that ΔLUMO becomes greater than ΔHOMO (Case C). Under these conditions, a positive-to-negative sign pattern in increasing energy is observed. The inversion of the sign pattern means that the angular momentum of the excited state is less than that of the ground state. Case C is rare in tetrapyrrole chemistry, but chlorophylls exhibit this pattern.

1.2.3   Optical Properties of Metallated vs. Free Base Porphyrins

Zinc tetraphenylporphyrin (ZnTPP) and free base tetraphenylporphyrin (H_2TPP) are the simplest synthetic porphyrins (Figure 1-7A). These two porphyrins can be used to briefly explain the connection between the absorption spectrum, MCD spectrum, and electronic structure.
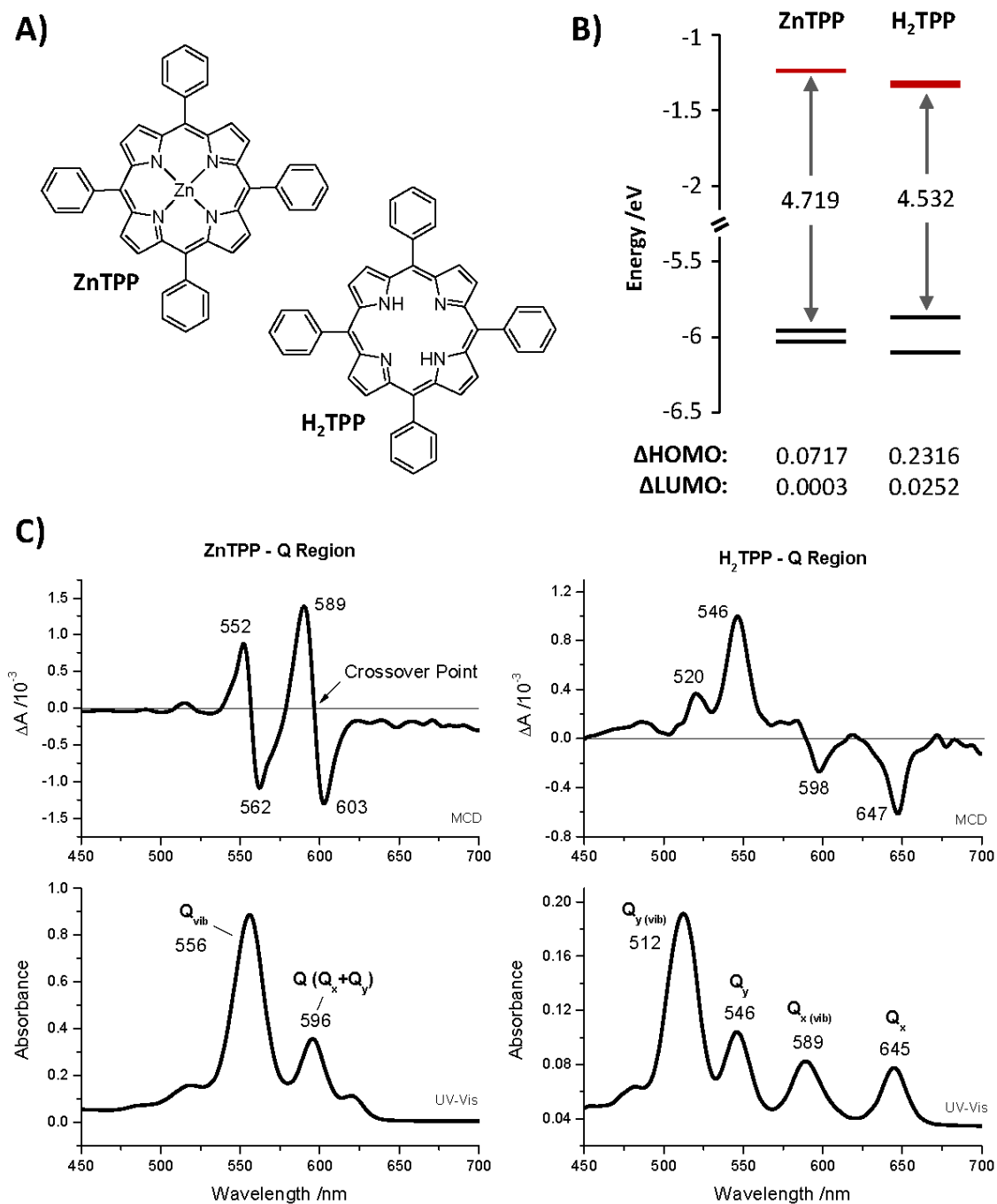
Figure 1-7 The structures (A) and Gouterman MO energies (B) of ZnTPP and H$_2$TPP. The HOMO pair is shown in black and the LUMO pair is shown in red. **(C)** MCD and absorption spectra of the Q region for ZnTPP (left) and H$_2$TPP (right). A$_1$ and B$_0$ terms are observed for ZnTPP and H$_2$TPP, respectively, in the MCD spectra.

Zinc is commonly used for the study of metallated porphyrins because it has a closed shell configuration (d^{10}). There will be no charge transfer contributions to the optical spectra. ZnTPP has D_{4h} symmetry while H_2TPP has D_{2h} symmetry. The lowered symmetry from D_{4h} to D_{2h} increases the splitting of the Gouterman MOs for H_2TPP. As observed in Figure 1-7B, the HOMO pair of ZnTPP are nearly degenerate while the LUMO pair are doubly degenerate. H_2TPP, with lower symmetry, exhibits larger ΔHOMO and ΔLUMO values than ZnTPP. These two porphyrins exhibit different spectral features due to the different degree of splitting between the Gouterman MOs (Figure 1-7C). The relatively larger ΔHOMO and ΔLUMO of H_2TPP lead to the separate observation of the Q_x and Q_y bands. The Q_x and Q_y bands of ZnTPP are superimposed. The respective vibronic bands are observed at lower wavelengths. Faraday A_1 terms (Case A) are observed in the MCD spectrum of ZnTPP, where the band is derivative shaped with the crossover point aligning with the associated absorption peak. Gaussian shaped B_0 terms (Case B) are observed in the H_2TPP MCD spectrum. Each band in the MCD spectrum corresponds to the respective absorption band. The experimental data supports the calculated energies of the Gouterman MOs in that ZnTPP has a degenerate excited state and H_2TPP has nondegenerate states.

1.3 Dye-Sensitized Solar Cells (DSSCs)

Due to the increasing demand for renewable energy, methods for solar energy to electricity conversion are of increasing importance. Traditional silicon-based solid-state solar cells are expensive and production is energy-intensive (high temperature and pressure processes) so efforts were made in developing nanocrystalline-based DSSCs.[23] DSSCs are cheaper and easier to fabricate than silicon-based solar cells but the power conversion efficiency (PCE) is still not as high.[24, 25] Different from traditional solar cells, light absorption and electron transport are handled by different materials in the cell.[23, 26, 27] This different mechanism allows for the tuning of the stability and optical properties of the sensitizing dye to maximize electron transfer to the wide-band-gap semiconductor, most often TiO_2 nanoparticles.
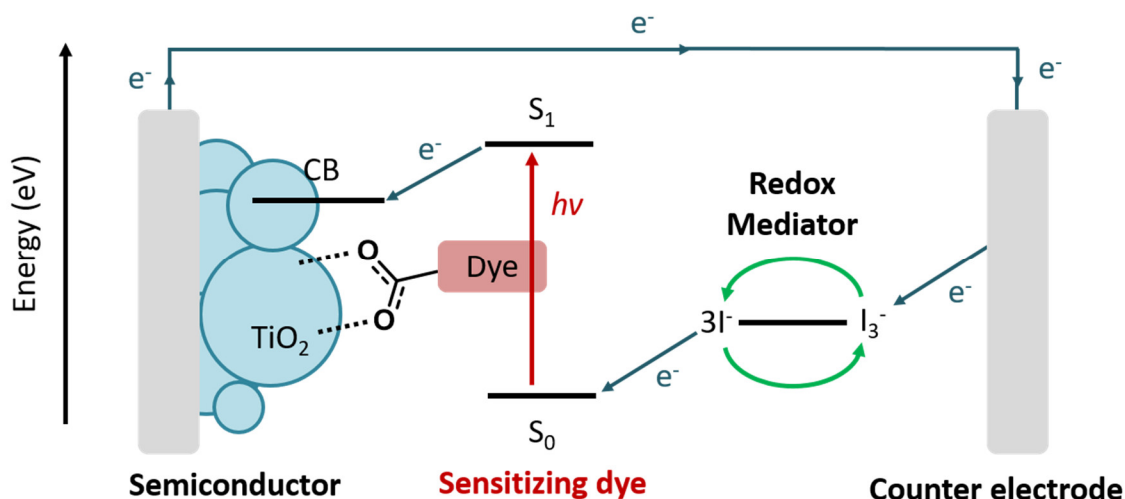
Figure 1-8 Components and operation principle of a DSSC.

DSSCs are composed of a sensitizing dye, a semiconductor (TiO$_2$ nanoparticles), an electrolyte (organic solvent containing iodide/triiodide redox mediator), and a counter electrode (Pt-coated).[28] A schematic diagram of its operating principles is shown in Figure 1-8. The dye is anchored to the semiconductor, usually through a carboxylic acid (COOH) group for porphyrins. Upon absorption of light by the dye, an electron is promoted from S$_0$ (ground) to S$_1$ (first excited state) and then transferred to the conduction band (CB) of the semiconductor. The oxidized dye is returned to its neutral state after reduction by iodide (I$^-$) and this process occurs rapidly to ensure that the excited electron, now on the CB, does not fall back into the ground state. The electron on the CB travels through an external circuit to the counter electrode and the circuit is completed when triiodide (I$_3^-$) is reduced to iodide at the counter electrode. The power conversion efficiency (PCE) of the DSSC is highly dependent on the sensitizing dye. An ideal dye should absorb all light in the visible and near-infrared (NIR) region (a panchromatic response) with strong absorption in the 700-900 nm region, have anchoring groups so it can bind strongly to the surface of the semiconductor, and be photostable so it can sustain many years of exposure to sunlight.[3] As well, the energy of the dye's excited state should lie just above the CB to minimize energy loss during the electron transfer.[27]

1.4 Tetrapyrroles as Sensitizers for DSSCs

Porphyrin and chlorin-based sensitizers have drawn great attention due to their structural analogy with the natural light-harvesting molecule, chlorophyll. Although these tetrapyrroles have strong absorption in the blue end of the visible region (B band), they do not normally absorb strongly in the red. However, they have a highly versatile structure which can be tuned to produce favourable spectroscopic and electrochemical properties.[3] Introducing electron donating and electron withdrawing groups (push-pull) and extending the π-conjugation system were found to improve the light harvesting ability for porphyrin dyes. The push-pull structure introduces a dipole within the HOMO and LUMO and facilitates electron transfer to the semiconductor. The HOMO will have electron density extended onto the donor group while the LUMO will have electron density extended onto the withdrawing group. The highest PCE of 13% was attained in 2014 using a porphyrin with the push-pull functionality.[24] Elongating the π-system lowers the HOMO-LUMO gap, which in turn shifts the Q band toward the NIR region.

1.5 Scope of Thesis

Chlorophylls are natural energy converters that exhibit an intense and red absorption band which is ideal for DSSC. However, chlorophylls cannot be used in applications because they are unstable. The goal of this project is to use the observed spectroscopic data and calculated electronic structure data of natural and fictive chlorophyll molecules to guide the design of stable tetrapyrrole dyes that show a panchromatic response with strong absorption in the red to NIR region. In this research, spectroscopic and computational studies were carried out on chlorophyll-derivatives, and synthetic and fictive porphyrins and chlorins. MCD spectroscopy is used to probe the relative angular momentum and orbital degeneracies of the ground and excited states. Density functional theory (DFT) and time-dependent DFT (TD-DFT) are used to provide further insight on the electronic structure and understanding of the spectroscopic data. The combination of computational methods with experimental data allows prediction of functionally relevant properties.

A strong absorption in the red to NIR region would require an intensification of the formally forbidden Q band and also a red-shift by around 100 nm. Previous reports by

Kobayashi and Stillman[19] showed that the splitting of the HOMO pair increased the intensity of the Q band. It is also known that the energy of the Q band is proportional to the HOMO-LUMO gap. The gap is decreased by the splitting of the four Gouterman MOs but these orbitals are normally degenerate for symmetrical porphyrins. The electronic structures of chlorophylls are examined in Chapter 3. Chlorophyll is found to have a split HOMO pair as well as a split LUMO pair, which is rarely observed. The splitting of the LUMO pair lowered the HOMO-LUMO gap more and resulted in a red-shifted Q band. The knowledge obtained from the analysis of chlorophyll substituents will be incorporated into the design of fictive porphyrins.

Chapter 4 reports a study of synthetic and fictive push-pull porphyrins. The substituents in the fictive porphyrins illustrate the differential effect of the donor and acceptor groups in the β-position of the pyrroles on the relative stabilities of the four Gouterman MOs. In Chapter 5, two fictive chlorins were designed based on a synthetic chlorin and previous findings on strong electron withdrawing and donating groups. The calculated parameters of these fictive tetrapyrroles are added to established trends that connect observable properties with computational results. This allows for the prediction of experimental properties for the fictive compounds and assessment of the computational results.

The electronic structures of zinc phthalocyanines[29], glutathione-dirhodium tetraacetate[30], a kite-tailed ZnTPP[31], and experimental studies on nano structures[32, 33] were also investigated. These results were reported as part of collaborative studies during the last two years. This thesis, however, will only focus on substituents that affect the electronic structure of porphyrins and chlorins to achieve an intense and red-shifted Q band.

<div align="center">Chapter 2</div>

2 Materials and Methods

2.1 Absorption and MCD Spectroscopy

UV-visible absorption data were recorded on a Varian Cary 500 absorption spectrometer (Varian, Toronto, Canada). MCD spectral data were recorded on a Jasco J-810 CD instrument (Jasco Inc., New Jersey, USA) with a 1.4 T permanent magnet (Olis Inc., Georgia, USA). All measurements were carried out at room temperature in a 1 cm quartz cuvette.

2.1.1 Preparation of Chlorophyll *a*

Chlorophyll *a* (Chl *a*) was extracted from spinach following the procedures outlined in the 2273a organic lab manual.[34] Spinach was purchased from the local grocery store and the leaves were ground in a food blender in petroleum ether. The pigments in spinach were separated with column chromatography using a 8:2 petroleum ether/acetone solvent mixture. The isolated Chl *a* was diluted with acetone for spectroscopic measurements. Baseline correction was carried out using acetone.

2.1.2 Preparation of Synthetic Porphyrins

The four synthetic porphyrins discussed in Chapter 4 were provided by Prof. Hong Wang, Miami University, Ohio, and their synthesis and characterization have been previously described.[35] The compounds were used as supplied. The sample solution was prepared by dissolving each compound in dichloromethane (DCM) (Caledon Laboratories Ltd). Baseline corrections were carried using DCM. The sample solutions were transferred into the same cuvette for measurement.

2.1.3 Preparation of Synthetic Chlorins

The three synthetic chlorins studied in Chapter 5 were kindly provided by Prof. Franz-Peter Montforts, Universität Bremen, and their synthesis and characterization are reported in the following papers.[36, 37] The compounds were used as supplied. The sample solutions for absorption and MCD spectroscopy were prepared by dissolving each compound in DCM.

2.2 Computational Methods

The Scigress Modelling Software (Fujitsu, Poland) was used to model all the compounds. A simple and quick geometry optimization using the PM5 semiempirical method was performed first in Scigress to clean up the structure. The PM5 calculations predict a planar structure for the tetrapyrrole ring.[38] The Gaussian G09 program[39] was used to carry out DFT and TD-DFT calculations. The DFT method uses the electron density distribution to compute the molecular orbitals and their respective energies. The TD-DFT method calculates the wave functions that oscillate between the ground and excited states at a single fixed geometry.[40] Ground state geometry optimizations, using the CAM-B3LYP functional and 6-31G(d,p) basis set, were performed to find the structural configuration with the minimum energy. CAM-B3LYP was chosen instead of B3LYP because it performs better with large aromatic molecules and in the presence of charge transfer excitations.[41] The basis set describes the shape of atomic orbitals (AOs) with wave functions. The AOs are linearly combined by the selected functional to generate molecular orbitals (MOs). TD-DFT calculations were performed on the optimized structures using the same functional and basis set to calculate the energies and MO contributions to the excited states and theoretical absorption spectra. The Polarizable Continuum Model (PCM) was used to model the solvent effects for the chlorophyll (Chapter 3) and chlorin compounds (Chapter 5). Water was chosen as the solvent for all chlorophyll calculations to best mimic the environment in the thylakoid membrane, which is better than calculation in vacuum. DCM was used for the chlorins. The porphyrins in Chapter 4 were calculated without the solvent parameter.

Chapter 3

3 Spectral and Electronic Properties of Chlorophyll

3.1 Introduction

Chlorophylls (Chls), comprising a chlorin macrocycle, exhibit intense and red absorption bands which are ideal properties for application in DSSCs. However, chlorophylls are not used in solar cells as the PCE is rather low and in addition, they are photochemically unstable.[42] The instability of the resulting chlorophyll cation radical, upon electron injection to the conduction band of the semiconductor, is susceptible to side reactions. Unlike in plants where the chlorophyll undergoes continuous turnover, the photosensitizer for DSSCs must be photostable to sustain many years of exposure to sunlight. To replace the functionality of the chlorophylls, it is necessary to design stable and atom efficient cyclic tetrapyrroles, for example porphyrins, chlorins, and phthalocyanines. Although we cannot use the chlorophyll ring itself in a device, studying its electronic structure provides a starting point for future design of tetrapyrrole-based dyes that exhibit ideal optical properties and photostability.

In this chapter, the relationship between the geometric structure and spectral properties of a number of chlorophylls are explored using DFT calculations. The electronic structure of a series of natural and fictive chlorophyll-derivatives were probed to determine the structural changes that resulted in the intense and red absorption property. Each of the natural chlorophylls shows splitting of the HOMO pair as well as significant splitting of the LUMO pair, which is rarely observed in porphyrins and phthalocyanines. Four fictive chlorophyll-derivatives were then designed and studied to probe the origin of the large ΔLUMO.

3.2 Results and Discussion

3.2.1 Natural Chlorophylls

The natural chlorophylls, *a*, *b*, *d*, and *f*, differ by the presence and position of the formyl group around the chlorin macrocycle (Figure 3-1). Despite this slight structural difference, these molecules exhibit quite different absorption properties. This difference in absorption

allowed photosynthetic organisms to use the most suitable Chl variation for light harvesting depending on the spectral distribution in their environment.[43] Chl *a* and *b* are found in plants while Chl *d* and *f* are found in cyanobacteria. The absorption and MCD spectra for chlorophylls have been reported many times previously.[44-46] For this thesis, only the experimental data of Chl *a* were collected. The nomenclature for chlorins and the spectroscopic axes for chlorophylls are shown in Figure 3-2.
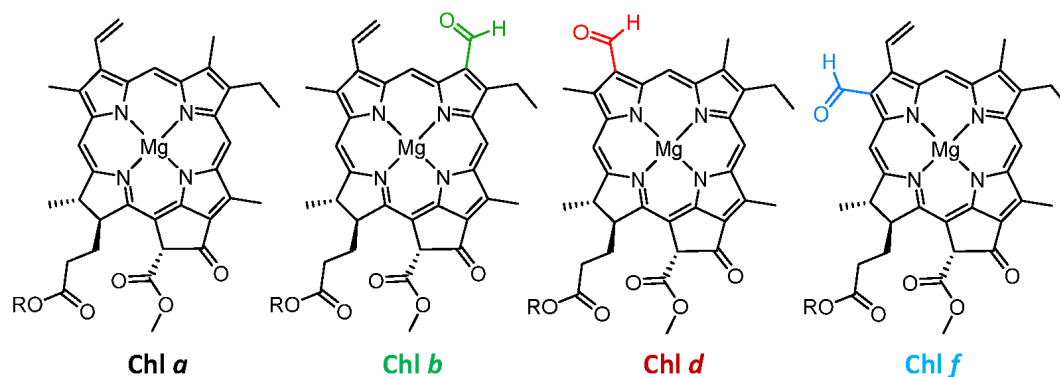
Figure 3-1 The structures of natural chlorophylls (Chls) a, b, d, and f (R = phytyl).
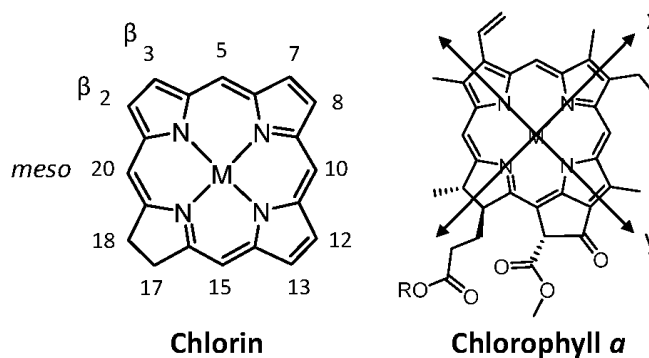
Figure 3-2 The nomenclature for chlorins (left) and spectroscopic axes for chlorophylls (right).

3.2.1.1 Optical Data of Chlorophyll *a*

The absorption, MCD, and calculated absorption spectra of Chl *a* are shown in Figure 3-3. In the absorption spectrum, the splitting of the Q_x and Q_y bands, along with the high intensity of the Q_y band, suggests that the magnitude of both ΔHOMO and ΔLUMO are large. Vibronic bands are observed at shorter wavelengths than their respective absorption

bands, at 615 nm for $Q_{y(vib)}$ and 530 nm for $Q_{x(vib)}$. In the MCD spectrum, B terms and a positive-to-negative sign pattern in increasing energy are observed. The positively signed 662 nm MCD B term locates the Q_y at 662 nm and the negatively signed 575 nm MCD B term locates the Q_x at 574 nm. This unusual sign pattern (positive-to-negative) indicates that chlorophyll exhibits a larger ΔLUMO than ΔHOMO. The B band region consists of a mixture of B_y, $B_{y(vib)}$, B_x, and $B_{x(vib)}$, as indicated by the multiple overlapping peaks in the absorption and MCD spectra. The MCD B region exhibits the same positive-to-negative sign pattern as that in the Q region.
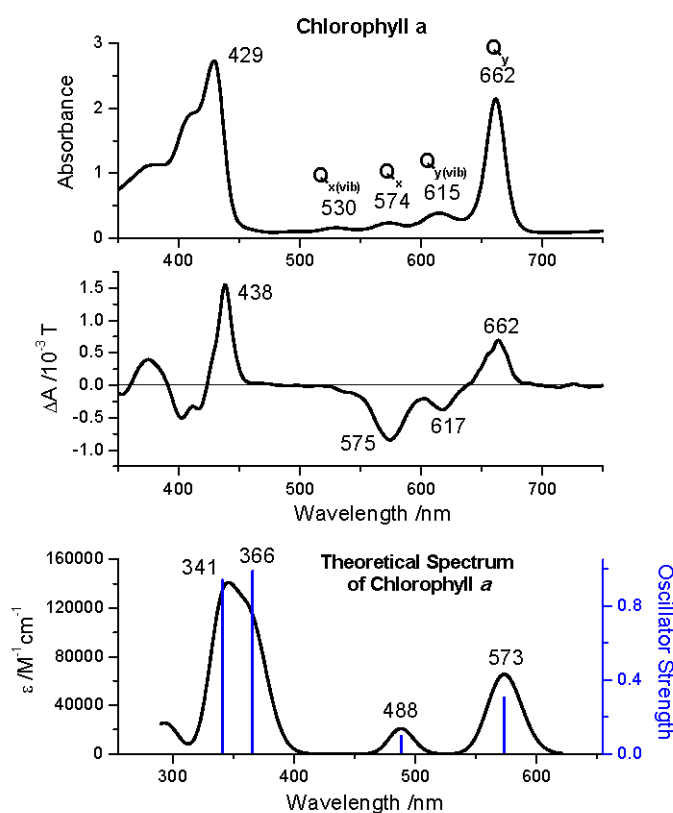
Figure 3-3 The absorption (top) and MCD (middle) spectra of Chl *a* in acetone. The calculated absorption spectrum for Chl *a* is shown in the last row.

The theoretical absorption spectrum does not contain vibronic bands as the calculations do not provide the excited state vibrational states. Because TD-DFT typically overestimates the excited state energies, the theoretical spectrum was plotted with different start and end x-axis values for better comparison with the experimental spectrum.

3.2.1.2   Electronic Structures of Natural Chlorophylls

The calculated absorption spectra and MO energies of the four Gouterman MOs for chlorophyll *a*, *b*, *d*, and *f* are shown in Figure 3-4. The TD-DFT data show that the electronic structure of chlorophyll has a large ΔHOMO and ΔLUMO, which resulted in the intense and red-shifted Q band. A trend formulated by Kobayashi and Stillman[19] showed that the intensity of the Q band is proportional to the magnitude of ΔHOMO. As well, another trend showed that the energy of the Q band is proportional to the HOMO-LUMO gap. For chlorophyll, the significant splitting of the LUMO pair decreased the HOMO-LUMO gap further, resulting in low energy Q bands which are ideal for application in DSSCs.
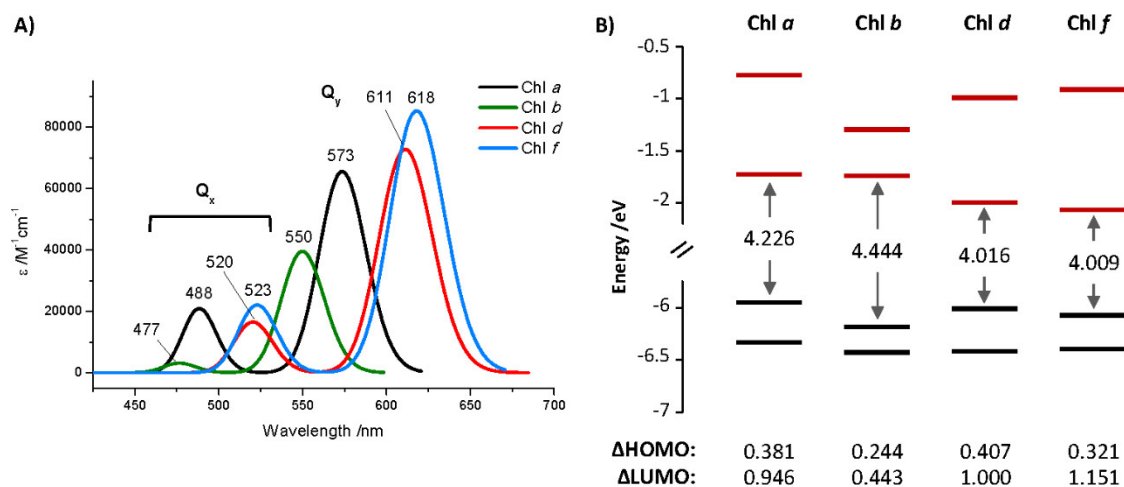
Figure 3-4 (A) The theoretical absorption spectra of the Q region of Chl *a* (573, 488 nm), *b* (550, 477 nm), *d* (611, 520 nm), and *f* (618, 532 nm). (B) The energy level diagram of the four Gouterman MOs, obtained from CAM-B3LYP/6-31G(d,p) DFT calculations. The LUMO pair is shown in red and the HOMO pair is shown in black.

The calculation is also consistent with the MCD result that Chl *a* has a ΔLUMO > ΔHOMO relationship. The change in sign pattern observed in the MCD spectrum is due to the change in angular momentum. Angular momentum of the degenerate orbitals decreases when they are split due to lowered symmetry. Since the LUMO pair are split more than the HOMO pair, the angular momentum of the LUMO pair becomes less than that of the HOMO pair. An electronic transition from a higher angular momentum to a lower angular momentum

orbital results in the reversed MCD sign pattern. It is unknown if this change in relative angular momentum has an effect on the chemistry of the molecule.

Chl *f*, with a formyl group along the y-axis (Figure 3-1), is observed to have the strongest and reddest Q band while Chl *b*, with a formyl group along the x-axis, is seen to have the weakest and bluest Q band. The calculated Q band order is consistent with the experimental order reported by Bocian *et al.*[44] A more red-shifted Q band corresponds to a smaller HOMO-LUMO gap. Comparison of the formyl-substituted chlorophylls with Chl *a* shows that the MO energies of the formyl substituted chlorophylls are all lower in energy. The ring π MOs increase in energy when they are electron rich and decrease in energy when they are electron deficient. The formyl group, being electron withdrawing, depletes the ring of density which lowers the energies of all the MOs. It is also observed that formyl substitution at the 2/3-positions (along the y-axis in Chl *d* and *f*) increased the splitting of the LUMO pair while formyl substitution at the 7-postion (along the x-axis in Chl *b*) decreased the magnitude of ΔLUMO. The larger splitting of the LUMO pair in Chl *f* results in a smaller HOMO-LUMO gap which corresponds to a redder Q band. It can be concluded from this that an electron withdrawing group along the y-axis of a chlorin will likely increase the splitting of LUMO and LUMO+1 while substitution along the x-axis will have the opposite effect.

The electron density surfaces of the four natural chlorophylls are shown in Figure 3-5. These surfaces provide a view of the electron distributions and show the nodes that identify the four Gouterman MOs: four for the HOMO pair and five for the LUMO pair. These surfaces also indicate the influence of peripheral substituents on the stability of the π system. In each of the MOs, little to no density is observed on the reduced pyrrole ring (positions 17 and 18). The electron withdrawing vinyl group at position 3 is delocalized with the π ring in the LUMO and LUMO+1 for each chlorophyll. In the Chl *f* LUMO, the additional electron withdrawing effect of the formyl group at position 2 results in the ring being more electron deficient than that of Chl *a*, *b*, and *d*. This stabilizes the LUMO further, increasing the magnitude of ΔLUMO (1.061 eV) and reducing the HOMO-LUMO gap (4.054 eV). The formyl group at position 7 in Chl *b* is able to interact with the LUMO+1 but does not interact with the LUMO because it lies on a node. The effect of the

delocalization with LUMO+1 lowers the energy of this MO, which in turn decreases the magnitude of ΔLUMO (0.466 eV) to less than that of Chl *a* (0.886 eV).

Figure 3-5 The electron density surfaces of the frontier MOs for Chl *a*, *b*, *d*, and *f*. Occupied MOs are coloured blue and green, unoccupied MOs are coloured red and yellow. Surfaces are shown with an isovalue of 0.02

3.2.2   Fictive Chlorophyll-Derivatives

When comparing the structure of chlorophyll to the porphyrin ring, it is observed that chlorophyll has a reduced pyrrole ring and a fifth ring that attaches to a methine bridge. To determine if these two structural changes contribute to the splitting of the LUMO and LUMO+1, which gave rise to a ΔLUMO > ΔHOMO relationship, chlorophyll derivatives **C1-C4** (Figure 3-6) were designed for analysis using DFT methods.
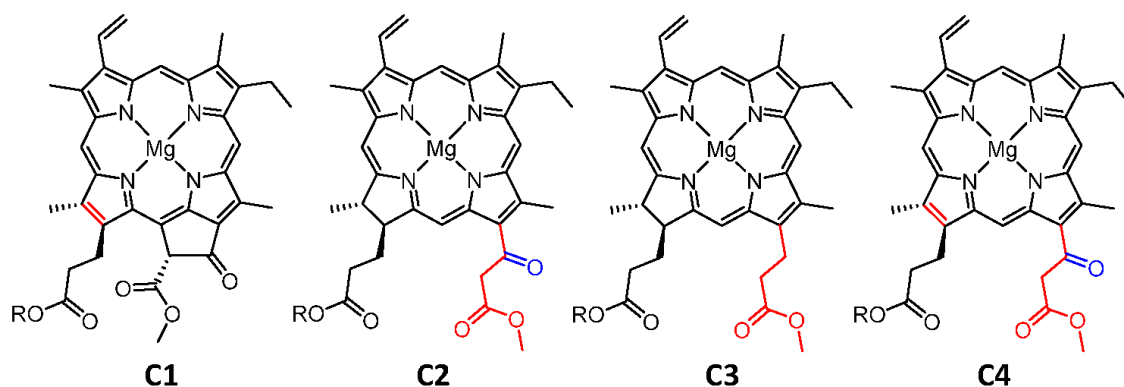
Figure 3-6 Structures of the fictive chlorophyll-derivatives, C1-C4.

The theoretical absorption spectra and Gouterman MO energies are shown in Figure 3-7. In **C1** where the pyrrole ring was oxidized and **C2** where the fifth ring was removed, the magnitude of ΔLUMO decreased when compared with the parent Chl *a*. The pyrrole reduction, however, was observed to have the most significant effect on the splitting of the LUMO pair. Reduction of the pyrrole reduces the π-electron conjugation of the ring, which destabilizes HOMO and LUMO+1 (each increases in energy) and results in a greater ΔHOMO and ΔLUMO (Figure 5-7B, Chl *a*). Molecule **C3** was tested to see the effect of the carbonyl group on the propionic side chain of the fifth ring on the value of ΔLUMO. Since **C3** without the carbonyl group exhibited a smaller ΔLUMO than **C2**, the presence of the extended π-conjugation from attached peripheral groups is confirmed to increase the magnitude of ΔLUMO. The presence of the fifth ring is observed to decrease the splitting of the HOMO pair while increasing the split between the LUMO pair when comparing the structures of Chl *a* with **C2** and **C1** with **C4**. As expected, the small ΔHOMO of **C1** and **C4** resulted in weak Q bands. The large ΔHOMO along with the large ΔLUMO of **C2** and **C3** lead to redder Q bands than **C1** and **C4**.
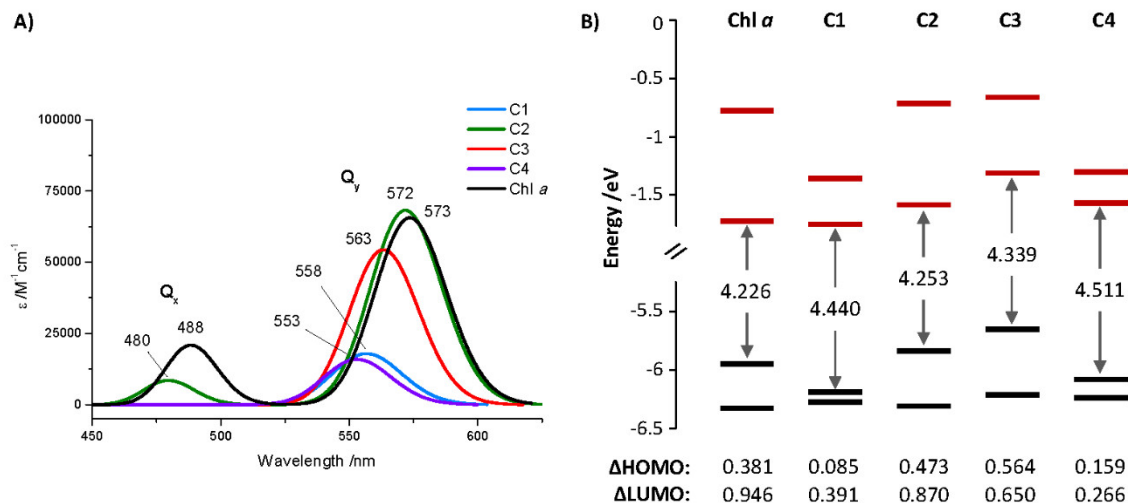
Figure 3-7 (A) Theoretical absorption spectra of the Q region and (B) energy level diagram of the Gouterman MOs for C1-C4. The data for Chl *a* are included for reference. The HOMO pair and LUMO pair are indicated with black and red lines, respectively.

The electron density surfaces shown in Figure 3-8 provide further insight into the differing energies of the Gouterman MOs. When the ring is completely unsaturated in **C1**, electron density is now observed on the previously reduced pyrrole in the HOMO and LUMO+1 (like a porphyrin). This stabilizes the HOMO and LUMO+1, decreasing the magnitudes of ΔHOMO and ΔLUMO, respectively. Comparing **C2** and **C3**, the presence of the electron withdrawing carbonyl group in **C2** lowers the energies of all the MOs by reducing electron density of the π ring. The carbonyl group is able to interact with the π ring LUMO, but not with LUMO+1 as it lies on a node. This stabilizes the LUMO of **C2** further than the LUMO of **C3**, resulting in a larger value of ΔLUMO for **C2**.
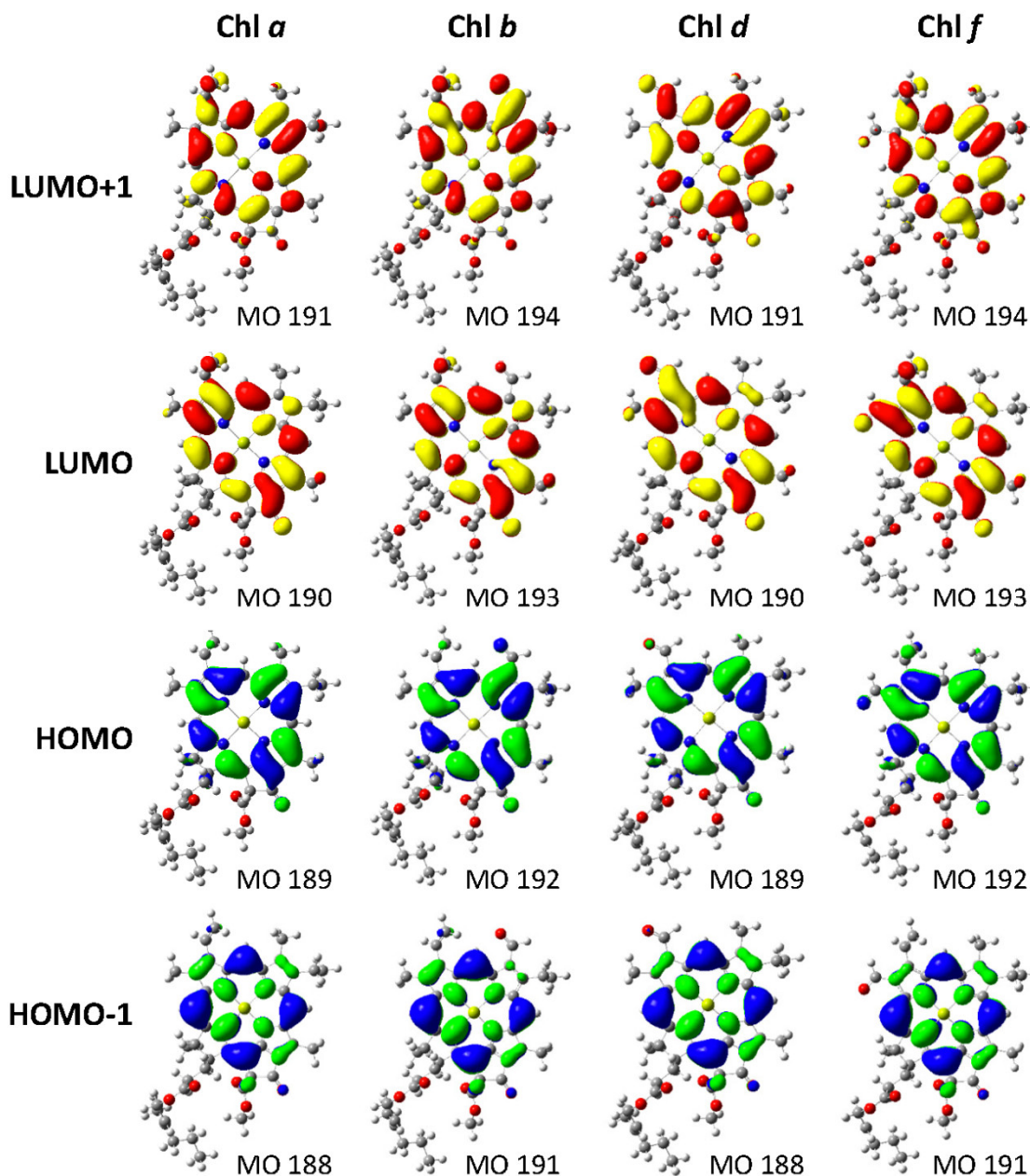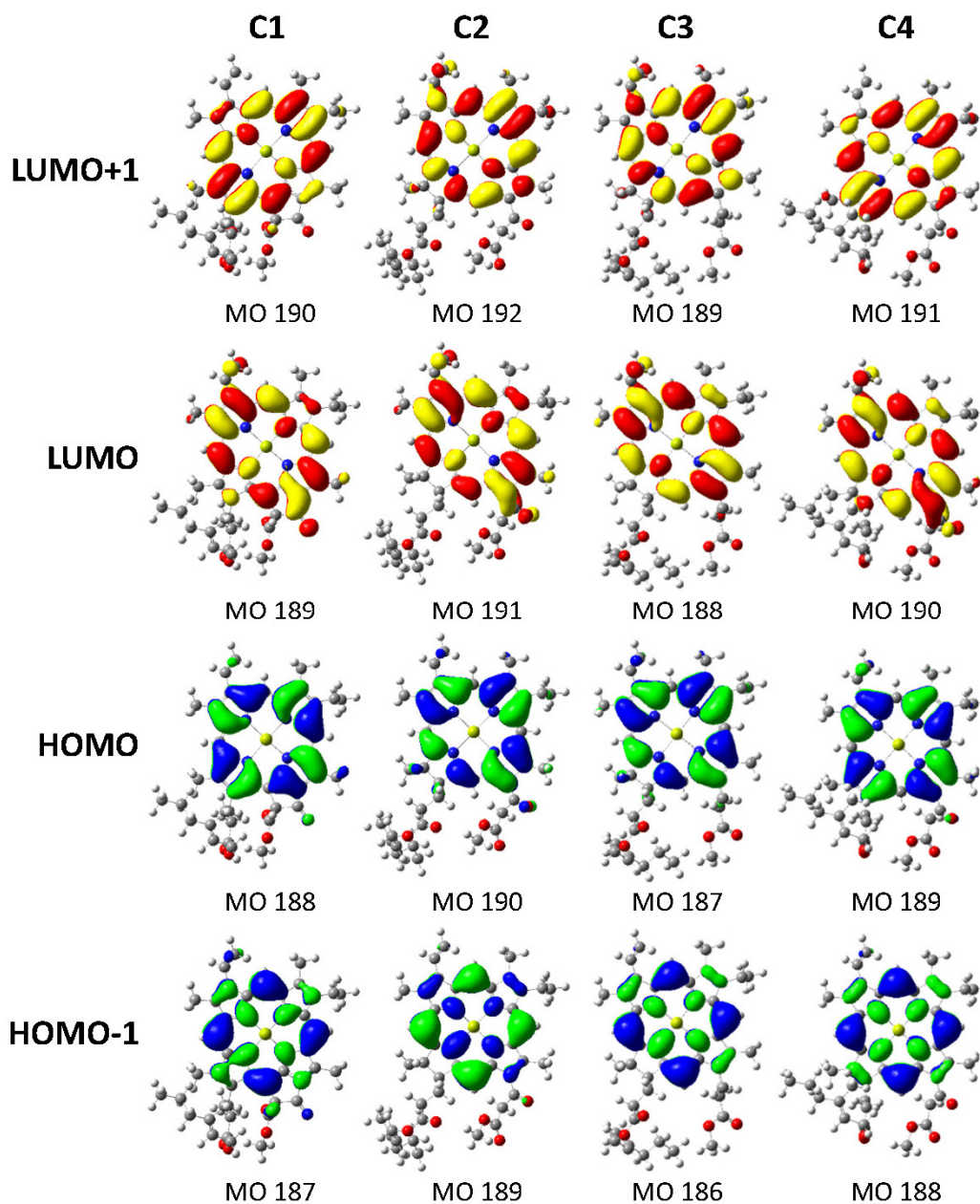
Figure 3-8 The electron density surfaces of the four Gouterman MOs for C1-C4.
Occupied MOs are coloured blue and green, unoccupied MOs are coloured red and yellow.

3.3   Conclusions

Nature has created different chlorophyll variations to accommodate the availability of
photon energy depending on the environment of the photosynthetic organism. Although
the chlorophylls are unstable and not suitable for use in DSSCs, Nature's modifications of

the tetrapyrrole ring to red-shift and intensify the Q band can be used to lead the design of synthetic dyes. The splitting of the HOMO pair intensified the Q band while the splitting of the LUMO pair further red-shifted the Q band. The splitting of the LUMO pair is rarely observed, therefore, the electronic structures of **C1-C4** were examined to determine the cause. The results showed that the splitting of the LUMO pair is achieved by reduction of the pyrrole ring, presence of the fifth ring, and position of the formyl group. For increased ΔLUMO and decreased HOMO-LUMO gap, it is necessary that the formyl group, or other electron withdrawing group, is located on the 2/3-positions of the chlorin ring (along the y-axis).

Chapter 4

4 Electronically Active β-Substituents on Porphyrins*

4.1 Introduction

The development of synthetic tetrapyrroles for DSSC application is of great current interest. Ever since the introduction of DSSCs by Grätzel and co-workers in 1991,[23] researchers have been looking for more efficient dyes to improve the efficiency of the solar cells. Two of the key requirements of an efficient dye is an intense and red absorbing band. Ruthenium-complex sensitizers were used for a long time due to their relatively high PCE (~12%).[47] However, the high cost and limited availability of ruthenium led to the investigation of organic-based dyes for DSSCs. Porphyrins and their derivatives are widely studied organic-based dyes owing to their wide spectral range, ease of modification, photochemical stability, and low toxicity.[3] For many years the PCE of porphyrin dyes remained below 10% because of low absorption in the red to NIR region. The introduction of extended π-conjugation and/or push-pull functionality has reduced this drawback. The highest PCE so far, of 13%, was achieved by a porphyrin with the push-pull functionality at the *meso*-position.[24]

In this chapter, the effect of electronically active β-substituents on the electronic structure of zinc porphyrins is described. The objective of the design of the synthetic porphyrins by Prof. Hong Wang, **1-4** (Figure 4-1), was to introduce push-pull substituents (electron donating and electron withdrawing, respectively) that would extend the π-conjugation, increase the splitting of the Gouterman MOs, red-shift the Q band, and introduce a dipole moment. MCD spectroscopy was used to support the results of computational analysis of the electronic states. The computational analysis provided an interpretation of why the Gouterman MOs split due to specific substitutions. Fictive porphyrins were then designed

_____

* A version of this Chapter has been published:

to explore the effect of simple electron withdrawing and donating groups on the splitting of the LUMO pair.

4.2 Results and Discussion

4.2.1 Synthetic Push-pull Porphyrins

The synthetic push-pull zinc tetratolylporphyrins were designed with a fused dimethoxybenzo group as an electron withdrawing group (EWG) on one pyrrole and on the opposite pyrrole, a single acetamido (**1**), a nitro (**2**), a proton (**3**), or a benzoylamino (**4**) substituent (Figure 4-1). The tolyl groups at the *meso*-positions are not in the plane of the porphyrin ring (they are perpendicular) so they do not interact with the π ring MOs. These groups decrease the possibility of aggregation and increase the solubility of the porphyrin.
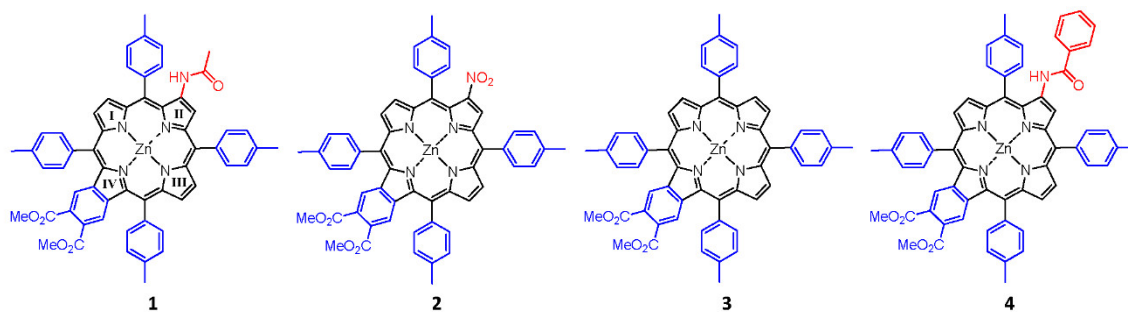
Figure 4-1 Structures of compounds 1-4. The porphyrins were substituted with dimethoxybenzo and an acetamido (**1**), a nitro (**2**), a proton (**3**), or a benzoylamino (**4**) group at the β-position on the opposite pyrrole. The four pyrroles are labeled I, II, III, IV in the structure of **1**.

4.2.1.1 The Optical Data of Compounds 1-4

The MCD, absorption, and theoretical spectra of compounds **1-4** are shown in Figure 4-2. The absorption spectra of all four compounds are typical of zinc tetraarylporphyrins (eg. ZnTPP),[19] where they have a weak Q band and the corresponding vibronic band (Q_{vib}) has higher intensity. The Q band of **2** is red-shifted by about 20 nm compared with **1**, **3**, and **4**, with Q at 614 nm and is the most intense of the four compounds.
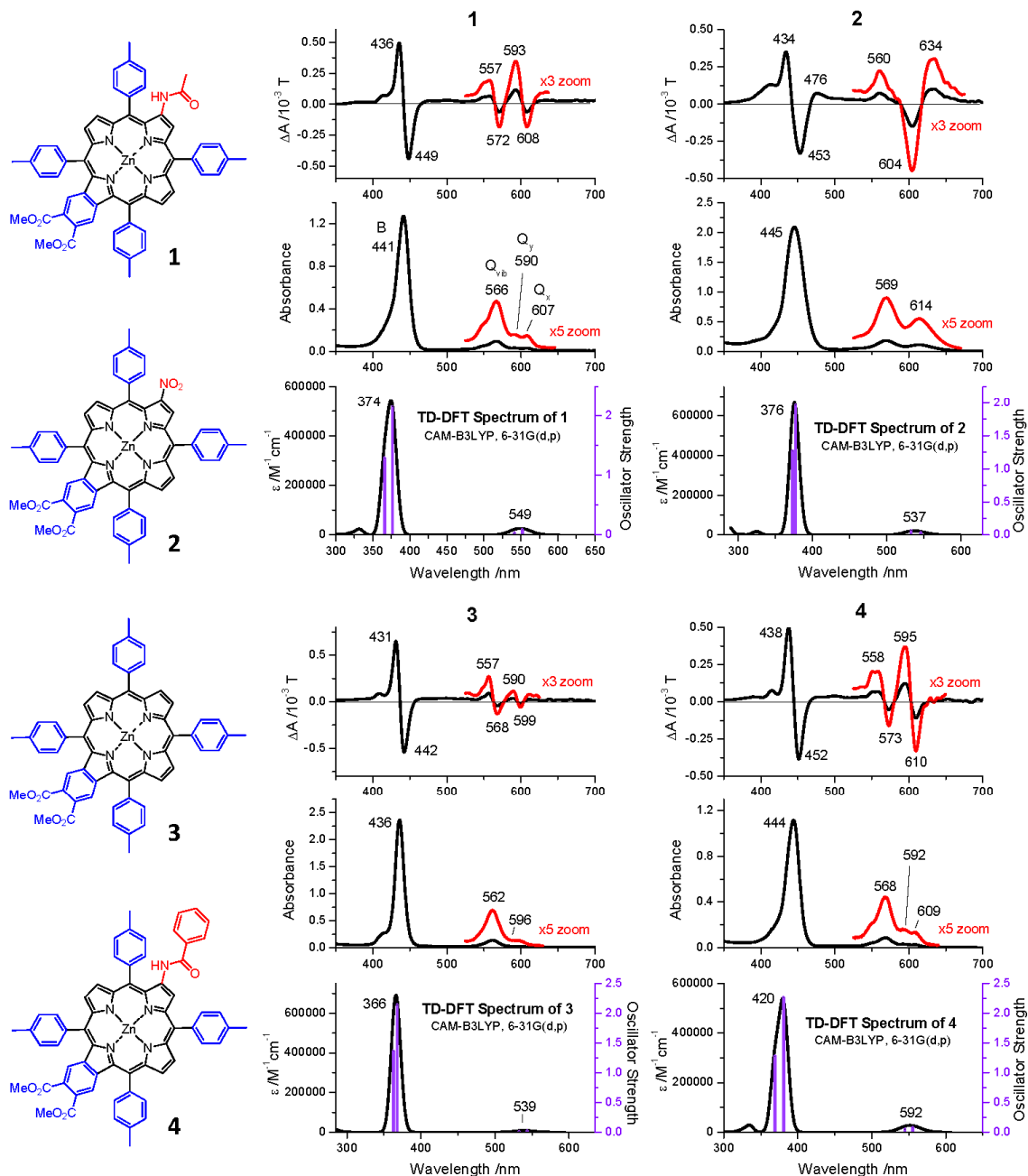
Figure 4-2 MCD, absorption, and calculated absorption spectra of 1, 2, 3, and 4. The Q region in the MCD and absorption spectra is enlarged by 3x and 5x respectively (red lines). In **1**, the splitting of the Q band is indicated by Q_y at 590 nm and Q_x at 607 nm. In the theoretical spectra shown in row 4, the very weak Q band and the B band are composed of two states, indicated by purple vertical lines.

The MCD spectra of **1**, **3**, and **4** (top row Figure 4-2) also follow the pattern for zinc tetraarylporphyrins, exhibiting the expected A_1 term with a negative-to-positive sign pattern. For **1** and **4**, the MCD spectra indicate that the Q band is actually split into its Q_x and Q_y components. Using 1 as an example, the negative 608 nm peak in the MCD spectrum corresponds to the 607 nm absorption band (Q_x) and the positive 593 nm MCD band corresponds to the absorption at 590 nm (Q_y). The vibronic band at 566 nm is observed to be composed of multiple transitions. Since the MCD band shape is observed to be like an A_1 term but Q_x and Q_y are split, the band shape is referred to as a "pseudo A term" where it is composed of equal and opposite B_0 terms. The MCD spectrum for **2** is different in that a positive-to-negative signed A_1 term is observed. This suggests that **2** exhibit a similar electronic structure to chlorophyll, where ΔLUMO is greater than ΔHOMO. It is impossible to tell with just the absorption spectrum that **2** has a different electronic structure than **1**.

The relative intensities of the B and Q absorption bands obtained from TD-DFT calculations agree well with the relative intensities observed in the experimental absorption spectra. Since the calculations overestimate the S_1 and S_2 energies, the theoretical spectra were plotted with different start and end x-axis to allow for better comparison with the experimental spectra.

4.2.1.2   The Electronic Structures of Compounds 1-4

The energies and electron density surfaces of the Gouterman MOs for compounds **1**-**4** are shown in Figures 4-3 and 4-4, respectively. The weak Q bands observed in the absorption spectra are a results of the small ΔHOMO. The calculated ΔHOMO values are also consistent with the experimental spectra, in that **1** and **4** have larger ΔHOMO values which gave rise to the splitting of Q_x and Q_y. Compound **2** is unusual because ΔLUMO is greater than ΔHOMO and its ΔHOMO is less than that of ZnTPP (0.07 eV). Comparing the structural differences between compounds **1**-**4**, it appears that the NO_2 group is likely the cause of this change in electronic structure. Although these compounds are able to split the typically degenerate LUMO pair, they are not likely to achieve high PCE in solar cells because this split is not large enough to decrease the HOMO-LUMO gap and bring S_1 closer to the CB of the semiconductor. It is interesting to note that the calculated HOMO-

LUMO gap for **2** (4.566 eV) is larger than that of **1** (4.467 eV). This suggest that the Q band for **2** is more blue-shifted than **1**, but the experimental spectra show that the Q band of **2** is more red than the Q band of **1**. It is possible that TD-DFT does not cope well with an electronic structure where the LUMO pair is split greater than the HOMO pair.
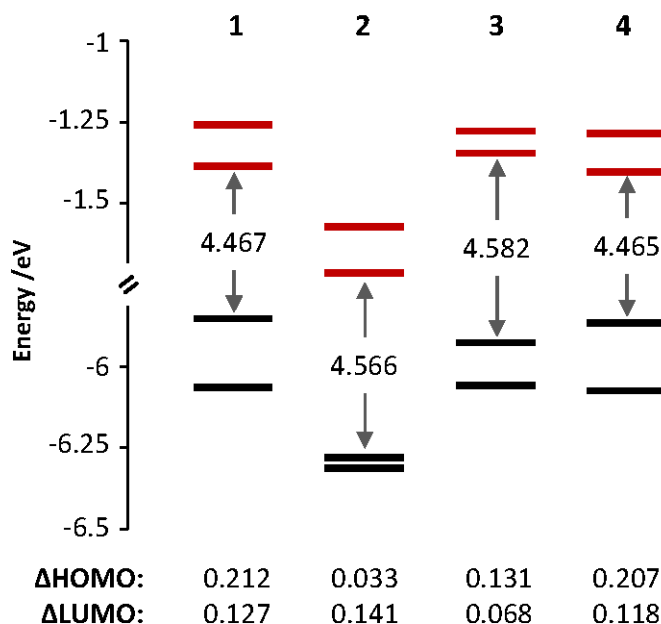
Figure 4-3 The energy level diagram of Gouterman's MOs for compounds 1-4.

The surfaces shown in Figure 4-4 provide a view of the electron distribution and show the nodal planes that identify the four Gouterman MOs. The acetamido (**1**), nitro (**2**), and benzoylamino (**4**) group at position 7 is seen to contribute density to the a_{1u} orbital (HOMO) but not the a_{2u} orbital (HOMO-1) since a node passes through it. Compared with just a proton at position 7 for **3**, the slightly electron donating acetamido and benzoylamino group adds density onto the HOMO of **1** and **4**, respectively, raising their energies and increasing the magnitudes of ΔHOMO. The electron withdrawing NO_2 group in **2** reduces density on the HOMO and brings it closer to HOMO-1. This effect decreases ΔHOMO significantly (0.033 eV) and results in it being less than ΔLUMO (0.141 eV). As well, the NO_2 group stabilizes the energies of all four orbitals compared with **1**, **3**, and **4**. Another significant feature is that the lowest energy e_g orbital for **1**, **3**, and **4** has nodal planes through pyrroles I and III (Figure 4-1) while this same orbital is LUMO+1 for **2**. Electron

density is observed on the NO$_2$ and dimethoxybenzo group in the LUMO, indicating that these groups can help facilitate electron transfer to the CB of the semiconductor.
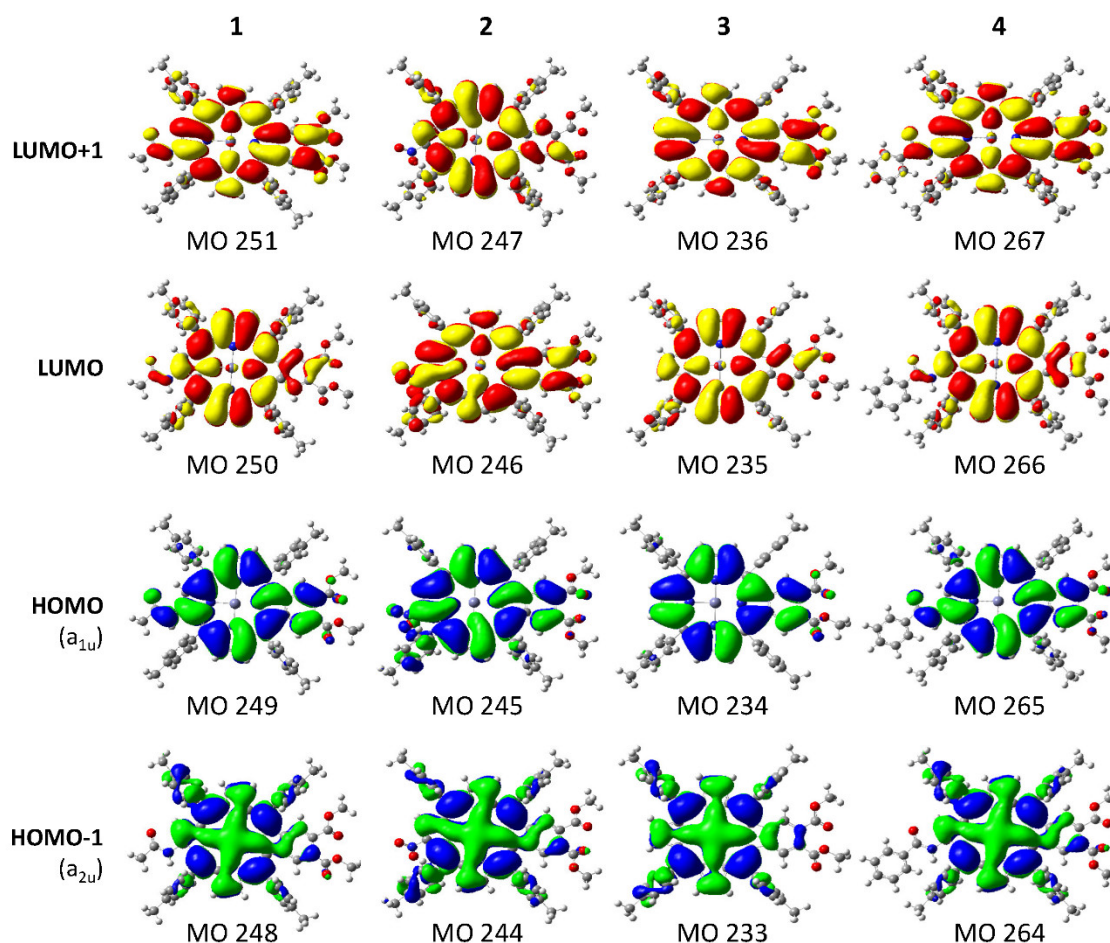
Figure 4-4 The electron density surfaces of the Gouterman MOs for compounds 1-4.

4.2.1.3   Origins of the Optical Spectra

Figure 4-5 shows the electronic transitions between the four Gouterman MOs that give rise to the Q$_x$ and Q$_y$ states. Since it is difficult to tell which band is x and which is y without a polarization experiment, the lower energy state is labeled as Q$_{-1}$ and the higher energy state is labeled as Q$_{+1}$. Q$_{-1}$ and Q$_{+1}$ arises from the transitions indicated by black lines and red lines, respectively (Figure 4-5). Table 4-1 provides the molecular orbital contributions to the states. The contribution percentages are calculated with the equation $2C^2 \times 100\%$, where C is the coefficient given by TD-DFT for each transition.

While the two states in **1**, **3**, and **4** show the typical combinations of tetraarylporphyrins involving two contributing transitions, each state in **2** unusually involves four transitions. The calculated optical spectra shown in row four in Figure 4-2 are all very similar, with the B and Q bands both consisting of two states each, with the relative intensities typical of tetraarylporphyrins. The optical spectra show no indication of the more complex nature of the excited state contribution for **2**.
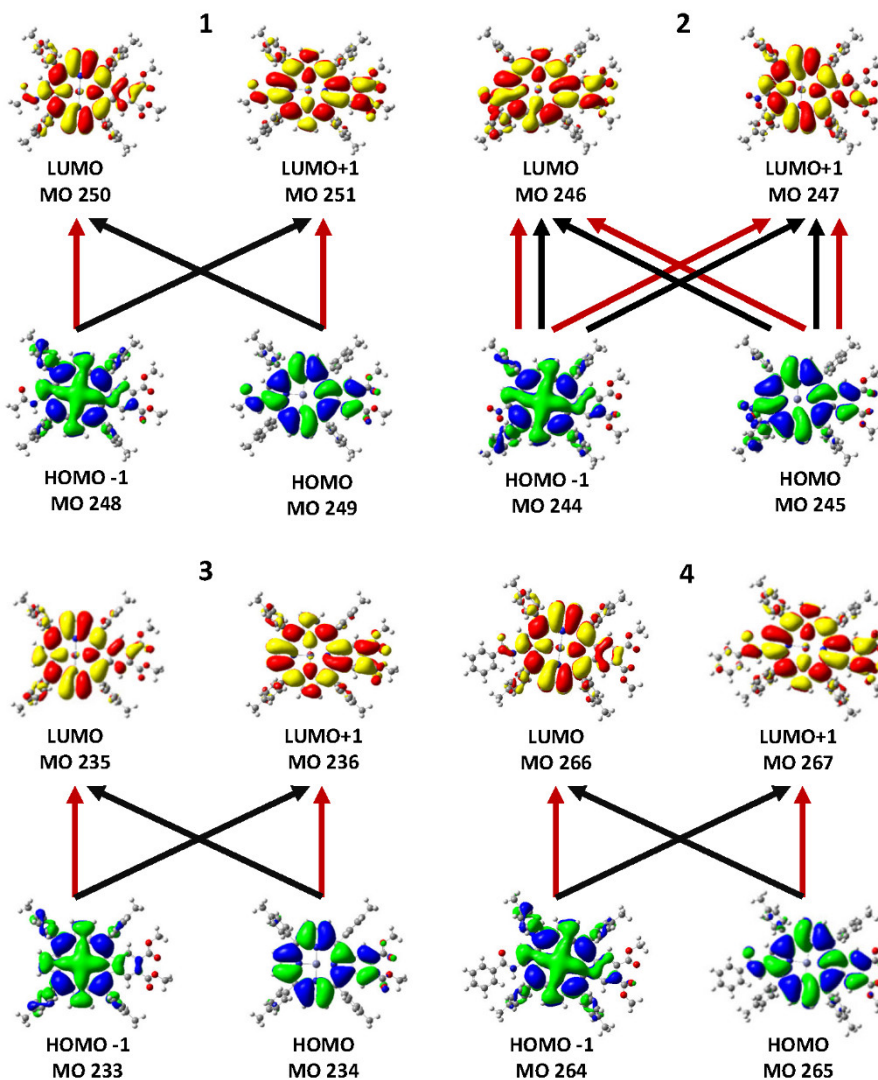
Figure 4-5 Major transitions between the four Gouterman MOs that give rise to the two Q band states obtained from TD-DFT calculations. Black lines are transitions that contribute to the lower excited state, Q_{-1}, and red lines show transitions that contribute to the higher excited state, Q_{+1}.

Table 4-1 Molecular orbital transitions to Q$_{-1}$ and Q$_{+1}$

Compound	State	State Energy /nm	f	Transition (Composition)
1	Q$_{-1}$	551.93	0.094	$248 \rightarrow 251$ (36%)
				$249 \rightarrow 250$ (62%)
	Q$_{+1}$	541.40	0.038	$248 \rightarrow 250$ (47%)
				$249 \rightarrow 251$ (51%)
2	Q$_{-1}$	546.06	0.041	$244 \rightarrow 246$ (31%)
				$244 \rightarrow 247$ (17%)
				$245 \rightarrow 246$ (21%)
				$245 \rightarrow 247$ (29%)
	Q$_{+1}$	532.94	0.069	$244 \rightarrow 246$ (21%)
				$244 \rightarrow 247$ (27%)
				$245 \rightarrow 246$ (34%)
				$245 \rightarrow 247$ (17%)
3	Q$_{-1}$	543.55	0.025	$233 \rightarrow 236$ (40%)
				$234 \rightarrow 235$ (57%)
	Q$_{+1}$	532.69	0.016	$233 \rightarrow 235$ (47%)
				$234 \rightarrow 236$ (50%)
4	Q$_{-1}$	553.08	0.086	$264 \rightarrow 267$ (35%)
				$265 \rightarrow 266$ (61%)
	Q$_{+1}$	542.73	0.050	$264 \rightarrow 266$ (45%)
				$265 \rightarrow 267$ (51%)

4.2.2   Fictive Porphyrins

Five fictive compounds, **F1**-**F5** (Figure 4-6), were designed with push and pull substituents to study the effect of electronically active β-substituted on the electronic structure. By substituting NO$_2$ at both β-positions on opposite pyrroles, **F1** mimics **2** in that both sides are electron withdrawing, although NO$_2$ is a stronger withdrawing group than the dimethoxybenzo group. For **F2**, one pyrrole was replaced with the electron donating NH$_2$ to achieve a push-pull functionality. For **F3** and **F4**, one pyrrole was substituted with two NH$_2$ groups and the opposite pyrrole was substituted with formyl (CHO) and carboxylic acid (COOH) groups, respectively. The formyl group was chosen because it is an important substituent in chlorophyll and carboxylic acid groups are the most commonly used anchor group for dye-sensitized solar cells.[27] Finally, **F5** was modelled to examine the effect of having the push-pull functionality on the *meso*- vs β-position.
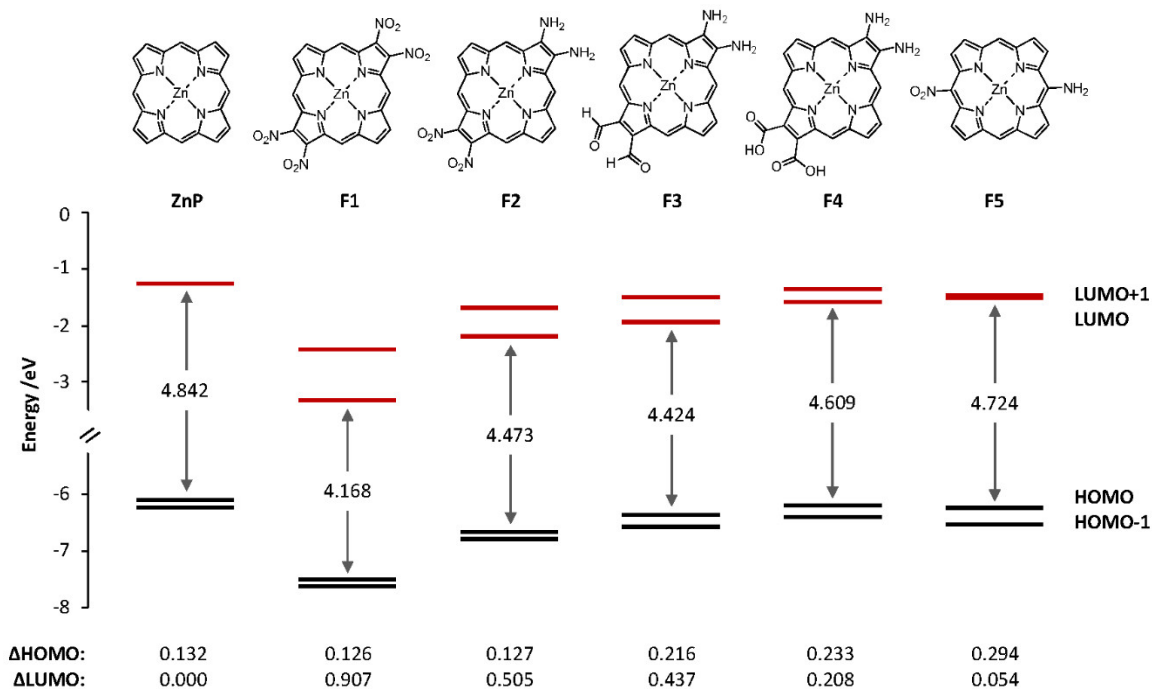
Figure 4-6 The structure, energy level diagram, and values of two HOMOs and two LUMOs in eV for the fictive molecules F1-F5. The frontier MO energies of ZnP are shown for comparision.

4.2.2.1   Electronic Structures

Figure 4-6 shows the energies of the four MOs for the five fictive compounds. The MO energies of zinc porphin (ZnP) is also shown for comparison. Being a symmetric molecule with D_{4h} symmetry, ZnP exhibits a degenerate pair of LUMOs and a nearly degenerate pair of HOMOs.

When electron withdrawing groups are installed on opposite pyrroles (**F1**), the LUMO pair is seen to split significantly while the HOMO pair remains nearly degenerate. Replacing the pull-pull functionality in **F1** with the push-pull functionality in **F2**, the value of ΔHOMO remained relatively the same but the magnitude of ΔLUMO became smaller (0.907 eV *versus* 0.505 eV). When NO_2 was exchanged for CHO and COOH as weaker electron withdrawing groups, ΔLUMO was seen to decrease while ΔHOMO increased. Interestingly, even though COOH (**F4**) is considered to be more electron withdrawing than CHO (**F3**), it had a smaller effect on the splitting of LUMO and LUMO+1 (0.208 eV *versus*

0.437 eV). This may be because the geometry optimized structure of **F4** had the COOH groups slightly tilted from the plane of the ring whereas the CHO groups in **F3** were planar. The slight tilt probably lowered the extent of π conjugation onto the COOH groups, resulting in a smaller ΔHOMO and ΔLUMO. Compounds **F1**-**F3** exhibited the rare relationship of ΔLUMO > ΔHOMO. Placing the push-pull functionality on the *meso*-position (**F5**) brought the LUMO pair back to near degeneracy. This means that the pyrrole β-position, which is along the x and y polarization axis, is a better substitution location for breaking the degeneracy of the LUMO pair. Compound **F1**, with the largest ΔLUMO, also has the smallest HOMO-LUMO gap which is expected since the stabilization of LUMO brought it closer to the HOMO, and therefore, its Q band will be the most red-shifted compared to the other fictive molecules.

4.2.2.2 Electron Density Surfaces

The electron density distribution of the four MOs for the fictive compounds is shown in Figure 4-7. For all the compounds, electron density is observed on the donating groups in the HOMO and on the withdrawing groups in the LUMO. The electron density differences between the excited and ground states are shown in the last row of Figure 4-7. It is easy to see from these images, that following photoexcitation, electron density is moving from the donor group (cyan) to the acceptor group (purple). This is a required property for a photosensitizer in dye-sensitized solar cells.
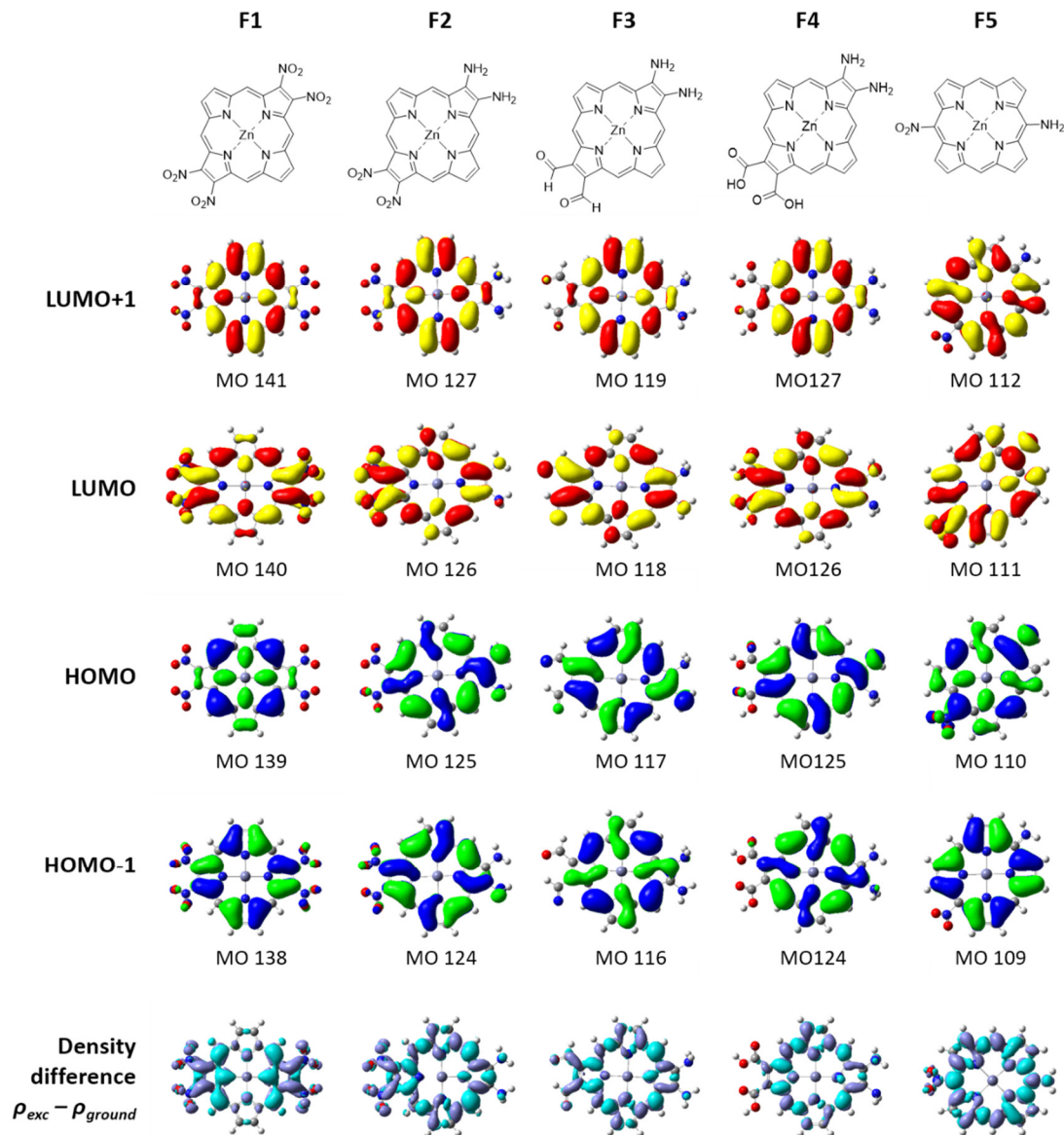
Figure 4-7 The electron density surfaces of the four MOs for F1-F5. The last row shows the density difference between the excited and ground states. Cyan represents where the electron is coming from and purple represents the direction in which the electrons are moving as a result of the excitation.

Analysis of the surfaces reveals that the HOMOs are not all of the same symmetry. The strength of the withdrawing group has a major effect on the energies of a_{1u} and a_{2u}. Because the nodes for a_{1u} lie on the pyrrole nitrogen atoms and methine bridges, its energy is heavily dependent on the substituent on the β-position. For **F1** and **F2**, the presence of the strongly

withdrawing NO_2 group pulls electron density from the ring and lowers the energy of a_{1u} below that of a_{2u}. The weaker withdrawing groups of formyl (**F3**) and carboxylic acid (**F4**) still pull electron density from the ring, but not enough to lower the energy of a_{1u} below a_{2u}.

4.2.3   Assessment of Computational Results

Computational data can provide an understanding of the underlying electronic structure that results in the observed optical and redox properties. However, the quality of the computational results is difficult to assess because the inaccuracies in the predicted properties must first be identified. Trends between the electronic structure and experimentally determined properties can be used as a way to assess the reliability of the computational results. A series of porphyrins and phthalocyanines from 2005 were used to formulate the trends.[19]

Figure 4-8 (A) Observed Q band energy *versus* the calculated HOMO-LUMO gap. (B) Calculated Q band oscillator strength, *f*, against the calculated ΔHOMO. The porphyrins and Pcs from 2005 are plotted as black circles. Red circles represent compounds **1-4** and blue triangles represent **F1-F5**. **(C)** Experimental *versus* calculated Q band wavelength. An expanded view of the plot for compounds **1-4** is included below.
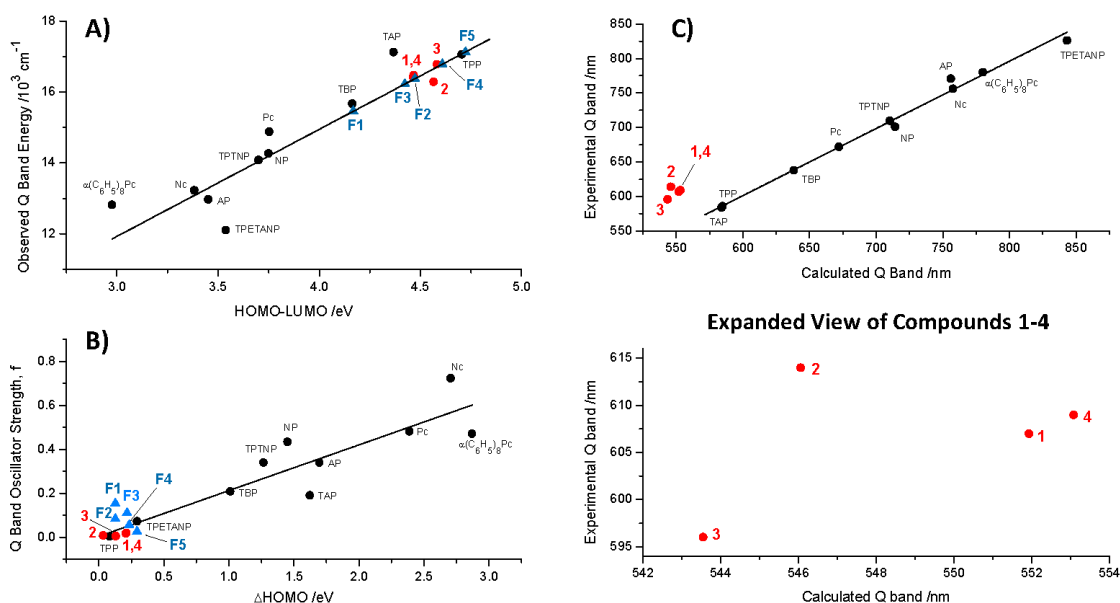
Figure 4-8A compares the Q band energy with the HOMO-LUMO gap. The use of the observed Q band as a function of the HOMO-LUMO gap energy removes the underlying errors in the calculation that may arise and introduce bias into the calculated data. The porphyrins and phthalocyanines used for the trend are complexes with purely extended π conjugation. The observed Q bands of **1-4** lie quite well on the trend line as shown in Figure 4-8A, suggesting that the calculated HOMO-LUMO gap matches with the experimental Q band energy no matter what the substitution. However, for application purposes, compounds **1-4** are not likely to achieve high PCE in solar cells because they have a large HOMO-LUMO gap which corresponds to a high energy Q band.

The fictive compounds are plotted using just the calculated HOMO-LUMO gap energies and placing the estimated Q band energy on the trend line. The slightly lower energy of **F3** *versus* **F2** suggests that formyl substitution might red-shift the Q bands more than the NO_2 substitution with the push of NH_2. Molecule F1, where both sides are electron withdrawing, exhibited the largest ΔLUMO and the smallest HOMO-LUMO gap which would result in the most red-shifted Q band. Having electron withdrawing groups on opposite sides also creates strong equal and opposite dipoles and this additional dipole moment can possible enhance the electron displacement onto the semiconductor.

Figure 4-8B shows a trend between the calculated oscillator strengths (*f*) and ΔHOMO. The magnitude of ΔHOMO is directly proportional to the Q band intensity. While determining the experimental values for *f* is not difficult for strongly absorbing tetrapyrroles, it is difficult to obtain reliable data for the weakly absorbing tetraphenyl compounds represented by **1**–**4** and **F1**–**F5** because the absorbance is so low. Thus, the calculated oscillator strengths are used for all the compounds in Figure 4-8B. The absorbance of the Q bands is very low for **1-4**, so the calculated values in 4-8B are likely to be good estimations of the experimental data. The key conclusion from 4-8B is that the peripheral substitution of **1**–**4** does not significantly split the accidental degeneracy of the HOMO pair, and therefore the Q band absorbance will be very weak.

Figure 4-8C compares the observed and calculated Q band energies. The linearity of the trend line obtained for the porphyrins and phthalocyanines from 2005 is convincing,

because although TD-DFT calculations overestimate the S_1 energy, resulting in blue-shifted Q band predictions, the error is systematic. On the other hand, the data for **1**–**4** consistently lie off the trend line. This might suggest that TD-DFT calculates the effect of having electron withdrawing and electron donating groups around the porphyrin ring in a manner that is different from a purely conjugated system. The expanded view of **1**–**4** shows that **2** lies well off the possible linear trend of **1**, **3**, and **4**. It is likely that the interaction of NO_2 with the π system resulted in a change in the π electronic structure and lead to the inaccurate calculation. This conclusion is supported by the effect the NO_2 substitution has on the LUMO pair.

4.3 Conclusions

The push-pull substituents modify the energies of the Gouterman MOs, which in turn influence the porphyrin's spectroscopic properties. The unusual positive-to-negative sign pattern in the MCD spectrum of compound **2** is due to a ΔLUMO greater than ΔHOMO relationship. This means that the angular momentum of the first excited state is less than that of the ground state and needs to be further studied in the future. Five fictive porphyrins were designed to illustrate the differential effect of the donor and acceptor groups at the β-position on the relative stabilities of the four Gouterman MOs. The computational studies showed that the NO_2 group resulted in the greatest splitting of the LUMO pair. The presence of strong electron withdrawing groups, such as NO_2 and formyl, opposite electron donating groups result in ΔLUMO > 0. This red-shifts the Q band and also introduces a dipole within the molecule, both of which are design objectives for photosensitizers. The use of calibrated trends provide a reliable way assessing the potential of a porphyrin for specific functions. By using experimental data from compounds with the same core structure, the optical properties of fictive compounds can be reliably predicted.

Chapter 5

5   Electronically Activated Chlorins*

5.1   Introduction

The increasing demand for renewable energy has led to the search for efficient methods for capturing photon energy and converting it into electricity. Dye-sensitized solar cells (DSSCs) are promising photovoltaic devices that mimic photosynthetic processes.[23] Chlorophylls (Chls) are Nature's energy convertors and the chlorin macrocycle (Figure 1-1) plays a major role in light-harvesting and the subsequent electron transfer.[48, 49] Nature's use of chlorophyll has inspired researchers to synthesize chlorin derivatives for use in DSSCs,[50, 51] as the natural Chls dimerize readily, and are also unstable.[52] A Chl *a* derivative with a long alkyl chain reported by Tamiaki *et al.* was able to achieve a PCE of 8%.[53]

The chlorin functionality is based on the reduced pyrrole ring, which gives a more intense and red-shifted lowest energy absorption band (Q band) when compared with the completely unsaturated porphyrin.[14] The tetrapyrrole macrocycle offers many design possibilities. Substituents can be attached to the pyrrole ring (β-position) and at the methine bridge (*meso*-position). As well, the absorption and redox properties of the π ring can be tuned by modifying the peripheral substituents, the conjugation pathway,[54, 55] and the central metal ion. Although chlorins provide much stronger and redder Q bands which are ideal for DSSCs, synthetic chlorins are difficult to make due to their lower symmetry and chemical stability compared with porphyrins.[56]

In this chapter, computational methods are used to guide the design of chlorin dyes that are predicted to exhibit favourable performance in DSSC applications. The individual influences of both β-substitution and Ni^{2+} coordination on the electronic structure of

---

* A version of this Chapter has been published:

chlorins were first explored through three synthetic chlorins (Figure 5-1). Computational studies on both the synthetic Ni^{2+} coordinated and modeled Zn^{2+} coordinated chlorins assisted in the assignment of the optical spectra and the interpretation of the effect of β-substitution with thioketone (**Syn3**), fluorene (**Syn6**), and ketone (**Lie95**). **Syn3** and **Syn6** exhibited the necessary intense, red Q band but lacked an anchor group for use in DSSCs. **Syn6** was used as the base of two fictive chlorins with thiophene units attached to the fluorene group. In addition, a donor group was incorporated in one of the fictive chlorins. The thiophene moiety from Yamamoto *et al.*[29] was utilized because thiophenes provide a good linking bridge between the tetrapyrrole and the anchor group that is necessary for connection to the semiconductor.[57] Polythiophene substituents in tetrapyrroles are known to increase the absorption coefficient and red-shift the Q band, which are necessary properties for efficient dyes.[58-60] MCD spectroscopy, DFT, and TD-DFT calculations were used to guide the design of the fictive chlorins. The effects of these substituents on the energies of the Gouterman MOs and the impact on the Q band energy and intensity were explored. The fictive chlorin with the donor group exhibited unique optical properties with a remarkably intense and red Q band which makes this compound an ideal candidate for use in DSSC applications.

5.2   Results and Discussion

5.2.1   Synthetic Chlorins

The three Ni^{2+} coordinated synthetic chlorins explored in this chapter were synthesized by Montforts *et al.* for possible application in DSSCs.[36, 37] The structures of **Syn3**, **Syn6**, and **Lie95**, are shown in Figure 5-1. The solutions (in DCM) of **Syn3** and **Syn6** were green while the solution of **Lie95** was blue.
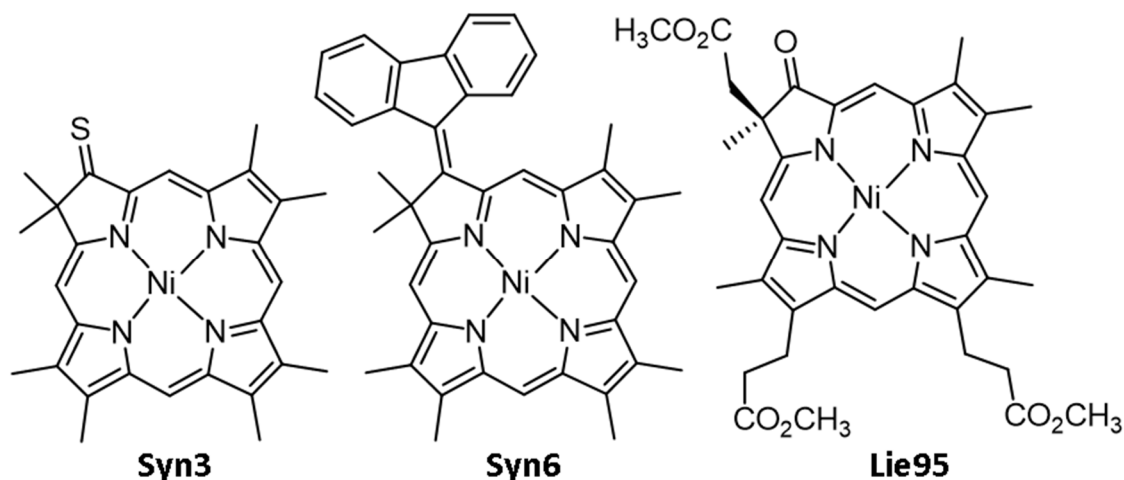
Figure 5-1 Structures of Syn3, Syn6, and Lie95.

5.2.1.1   UV-Visible Absorption and MCD Spectral Data

The absorption and MCD spectra for the three Ni^{2+} coordinated chlorins are shown in Figure 5-2. For each of the three chlorins, four bands are observed in the Q band region: Q_x, Q_y, and their respective vibronic bands. The splitting of Q_x and Q_y suggests that the magnitudes of ΔHOMO and ΔLUMO are large.[19, 61] A negatively signed MCD B term locates Q_x at 684, 680, and 612 nm for **Syn3**, **Syn6**, and **Lie95**, respectively. A positively signed MCD B term locates Q_y at 591, 586, and 544 nm for **Syn3**, **Syn6**, and **Lie95**, respectively. The negative-to-positive sign sequence of the B terms indicates that ΔHOMO is larger than ΔLUMO in all three chlorins.[9, 22]

Figure 5-2 MCD, absorption, and calculated absorption spectra for the Ni-coordinated Syn3, Syn6, and Lie95 in DCM. The theoretical spectra of the respective Zn-coordinated chlorins are shown in the last row.

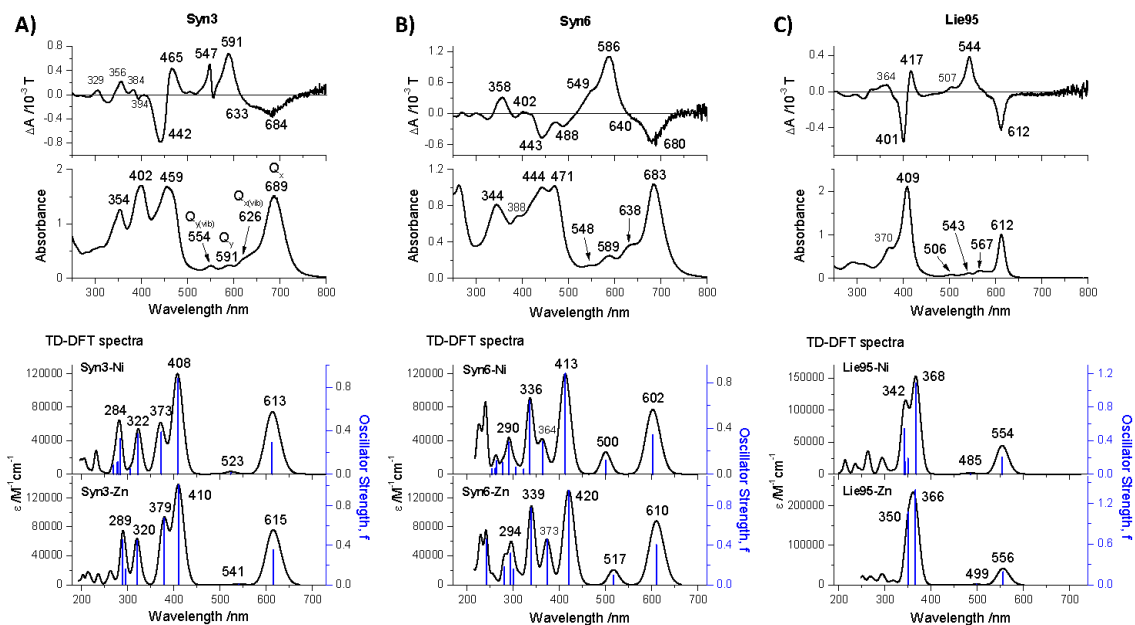Multiple bands are observed in the B band absorption region for **Syn3** and **Syn6** while a typical single B band is observed for **Lie95**. The panchromatic absorption as a result of multiple transitions in the B band region, along with the intense red-shifted Q band for **Syn3** and **Syn6** would likely make these more efficient sensitizing dyes than **Lie95**.

The theoretical spectra of the Ni^{2+} and Zn^{2+} coordinated complexes are also included in Figure 5-2 to allow for direct comparison with the experimental data. TD-DFT calculations overestimate the energies of the excited states.[62, 63] To allow for easier band assignment between the theoretical and experimental spectra, different start and end values of the x-axis were chosen for the theoretical spectra. From the calculations, the lowest energy Q band was found to be Q_x for **Syn3**, **Syn6**, and **Lie95**. This is opposite the case for chlorophyll, where Q_y is the lowest energy absorption band.[16, 17] **Syn3** and **Syn6**, with the thioketone and fluorene substitution, respectively, exhibit experimental Q bands (at 689 and 683 nm, respectively) that are more red-shifted than chlorophyll *a* (662 nm).

5.2.1.2 Influence of Ni^{2+} on the Optical Spectra

Ni^{2+} has unfilled d-orbitals (d^8) which allows for charge transfer to the ring MOs and vice versa. Zn^{2+}, with completely filled d-orbitals (d^{10}), will not exhibit charge transfer contributions to the optical spectra in the visible region. Tables 5-1 to 5-3 shows a comparison of the excited state contributions for the Zn- and Ni-centered synthetic chlorins. For the Zn-centered **Syn3**, **Syn6**, and **Lie95**, excited states 1 and 2 represent the Q$_x$ and Q$_y$ bands and arise from the usual set of transitions between the four Gouterman MOs. On the other hand for the Ni-centered compounds, the calculations show excited states from charge transfer and d–d transitions at lower energies of the Q band. However, transition to these states have oscillator strengths close to zero. The transitions that make up the Q and B bands come from similar MOs for both the Zn-and Ni-centered compounds, except in addition, the Ni-centered compounds exhibit ring to metal, metal to ring, and ring to substituent transitions. The electron density surfaces for the non Gouterman MOs are shown in Appendix A-C.

Table 5-1 Molecular orbital contributions to the excited states for Syn3. Gouterman MOs are highlighted in red. Only states with $f > 0.01$ are shown, except for the states before the Q band in the Ni-Centered compounds

| Chlorin | Zn | | | | Ni | | | |
	State	State Energy /nm	f	Transition (contribution)	State	State Energy /nm	f	Transition (contribution)
Syn3	1 (Q)	615.27	0.349	134→137 (11%) 135→136 (88%)	1	670.10	0.000	128→138 (4%) 129→138 (98%) 129←138 (4%)
	2 (Q)	540.77	0.005	134→136 (54%) 135→137 (45%)	2	641.62	0.000	123→138 (3%) 125→138 (42%) 132→138 (52%)
	4 (B)	409.83	1.010	134→136 (42%) 134→138 (4%) 135→137 (50%)	3	616.99	0.054	124→138 (20%) 126→138 (21%) 128→138 (4%) 130→138 (34%) 134→135 (14%)
	5 (B)	378.80	0.674	134→136 (3%) 134→137 (66%) 135→136 (10%) 135→138 (17%)	4 (Q)	612.62	0.291	124→138 (4%) 126→138 (4%) 130→138 (6%) 133→136 (7%) 134→135 (76%)
					5 (Q)	523.39	0.014	133→135 (47%) 134→136 (50%)
					8 (B)	407.97	0.878	133→135 (47%) 133→137 (2%) 134→136 (45%)
					10 (B)	372.61	0.385	130→135 (8%)

State	Energy	f	Transition
			132→136 (5%)
			133→135 (4%)
			133→136 (55%)
			134→135 (6%)
			134→137 (16%)
12	363.22	0.104	126→135 (2%)
			130→135 (74%)
			130→137 (4%)
			132→136 (3%)
			133→136 (6%)
			134→137 (4%)
14	330.87	0.050	128→135 (6%)
			130→136 (7%)
			132→135 (14%)
			132→136 (57%)
			133→136 (6%)
15 (B)	322.37	0.368	128→135 (5%)
			132→135 (3%)
			133→136 (16%)
			134→137 (66%)

Table 5-2 Molecular orbital contributions to the excited states for Syn6. Gouterman MOs are highlighted in red. Only states with $f > 0.01$ are shown, except for the states before the Q band in the Ni-Centered compounds

Chlorin	Zn				Ni			
	State	State Energy /nm	f	Transition (contribution)	State	State Energy /nm	f	Transition (contribution)
Syn6	1 (Q)	609.97	0.405	169→172 (9%) 170→171 (87%)	1	625.90	0.000	162→174 (8%) 163→174 (91%) 163←174 (4%)
	2 (Q)	517.24	0.096	169→171 (29%) 170→172 (64%)	2	609.45	0.010	156→174 (5%) 158→174 (24%) 159→174 (11%) 164→174 (12%) 165→174 (20%) 167→174 (21%) 169→170 (3%)
	3 (B)	420.14	0.957	168→171 (6%) 168→172 (3%) 169→171 (46%) 169→172 (7%) 170→172 (23%) 170→173 (11%)	3 (Q)	602.16	0.343	168→171 (7%) 169→170 (86%)
	4 (B)	373.01	0.460	168→171 (2%) 169→171 (18%) 169→172 (44%) 170→171 (6%) 170→172 (5%) 170→173 (20%)	4	587.23	0.006	157→174 (19%) 158→174 (4%) 160→174 (27%) 162→174 (3%) 164→174 (9%) 165→174 (23%) 167→174 (7%) 168→174 (3%)
	7 (B)	339.48	0.775	164→171 (3%) 169→172 (32%) 170→171 (3%) 170→173 (55%)	5 (Q)	500.27	0.122	168→170 (26%) 169→171 (67%) 169→172 (2%)

State	State Energy /nm	f	Transition (contribution)
7 (B)	412.70	0.878	167→170 (7%)
			167→171 (2%)
			168→170 (48%)
			168→171 (4%)
			169→171 (21%)
			169→172 (11%)
8	388.72	0.055	164→170 (9%)
			164→171 (3%)
			165→170 (25%)
			165→171 (2%)
			167→170 (41%)
			167→171 (8%)
			168→170 (3%)
			169→171 (2%)
9 (B)	363.94	0.283	167→171 (3%)
			168→170 (17%)
			168→171 (32%)
			169→170 (4%)
			169→171 (2%)
			169→172 (34%)
			169→174 (2%)
11	350.67	0.054	160→170 (2%)
			164→170 (4%)
			165→170 (32%)
			167→170 (8%)
			168→171 (4%)
			169→174 (40%)
14 (B)	336.16	0.639	168→171 (42%)
			169→170 (3%)
			169→172 (43%)
			169→174 (5%)

Table 5-3 Molecular orbital contributions to the excited states for Lie95. Gouterman MOs are highlighted in red. Only states with $f > 0.01$ are shown, except for the states before the Q band in the Ni-Centered compounds

	Zn				Ni			
Chlorin	State	State Energy /nm	f	Transition (contribution)	State	State Energy /nm	f	Transition (contribution)
Lie95	1 (Q)	555.84	0.190	179→182 (17%) 180→181 (82%)	1	671.50	0.000	175→183 (100%) 175←183 (5%)
	2 (Q)	498.69	0.006	179→181 (49%) 180→182 (50%)	2	642.41	0.000	167→183 (4%) 168→183 (9%) 169→183 (12%) 170→183 (13%) 171→183 (5%) 177→183 (54%)
	3 (B)	365.86	1.394	179→181 (49%) 180→182 (48%)	3	619.24	0.000	167→183 (6%) 168→183 (10%) 169→183 (6%) 172→183 (29%) 174→183 (4%) 176→183 (37%) 178→183 (4%)
	5 (B)	350.5	1.074	179→182 (78%) 180→181 (18%)	4 (Q)	553.99	0.205	178→181 (13%) 179→180 (87%)

5 (Q)	485.43	0.010	178→180 (46%)
			179→181 (52%)
8 (B)	367.64	1.084	176→180 (2%)
			178→180 (48%)
			179→181 (45%)
10	349.93	0.188	176→180 (52%)
			177→181 (5%)
			178→181 (23%)
			179→180 (4%)
			179→182 (3%)
			179→183 (4%)
11	343.85	0.149	178→181 (14%)
			179→180 (2%)
			179→183 (81%)
12 (B)	342.11	0.543	176→180 (26%)
			178→181 (43%)
			179→180 (6%)
			179→182 (2%)
			179→183 (11%)

5.2.1.3   The Electronic Structures of Syn3, Syn6, and Lie95

The energies and electron density surfaces of the four Gouterman MOs obtained from DFT and TD-DFT calculations for the Ni- and Zn-coordinated **Syn3**, **Syn6**, and **Lie95** are shown in Figure 5-3 and 5-4. Data for the unsubstituted Ni and Zn chlorin are also shown for comparison.
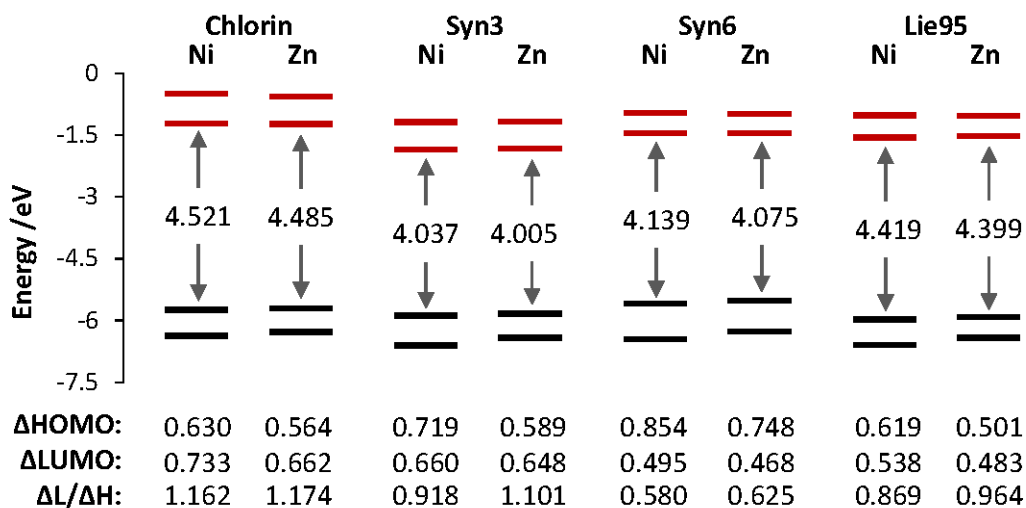
Figure 5-3 The energy levels of Gouterman's four MOs obtained from CAM-B3LYP/6-31G(d,p) DFT calculations. The last row shows the ratio between ΔLUMO/ΔHOMO. A value greater than 1 indicates that ΔLUMO > ΔHOMO.

The reduced symmetry of the chlorin compared with a porphyrin, due to the reduced pyrrole ring, splits the typically degenerate HOMO pair and LUMO pair (Figure 5-3). In comparison with the unsubstituted zinc chlorin, the electron withdrawing nature of the thioketone (**Syn3**), fluorene (**Syn6**), and ketone (**Lie95**) groups at the β-positions stabilize the Gouterman MOs, lowering their energy. **Syn3**, with the strongest electron withdrawing group of the three chlorins (thioketone), exhibited the largest decrease in orbital energy. The fluorene group shows the smallest electron withdrawing character of the three, based on the reduction in MO energy. The Zn-centered compounds exhibit smaller HOMO– LUMO gaps, resulting in a more red-shifted Q band than the respective Ni-centered compounds in the computed absorption spectra. Interestingly, only the Zn-centered **Syn3** exhibited a ΔLUMO > ΔHOMO relationship like the parent chlorin. The surfaces in Figure 5-4 help explain this difference. The LUMO pair with five nodes experience similar electron densities so the metal will have no major effect on their energies. The a_{1u} orbital (HOMO) has nodes through the pyrrole nitrogen and the metal, making it also insensitive to the metal. However, the density surface for the a_{2u} orbital (HOMO-1) shows contributions from the Ni^{2+} d-orbitals that are absent for the Zn complexes, which results in the a_{2u} ring orbital being stabilized. Therefore, when the chlorins are Ni-coordinated, the metal stabilizes HOMO-1 and results in a ΔHOMO that is larger than the respective Zn-coordinated chlorin.
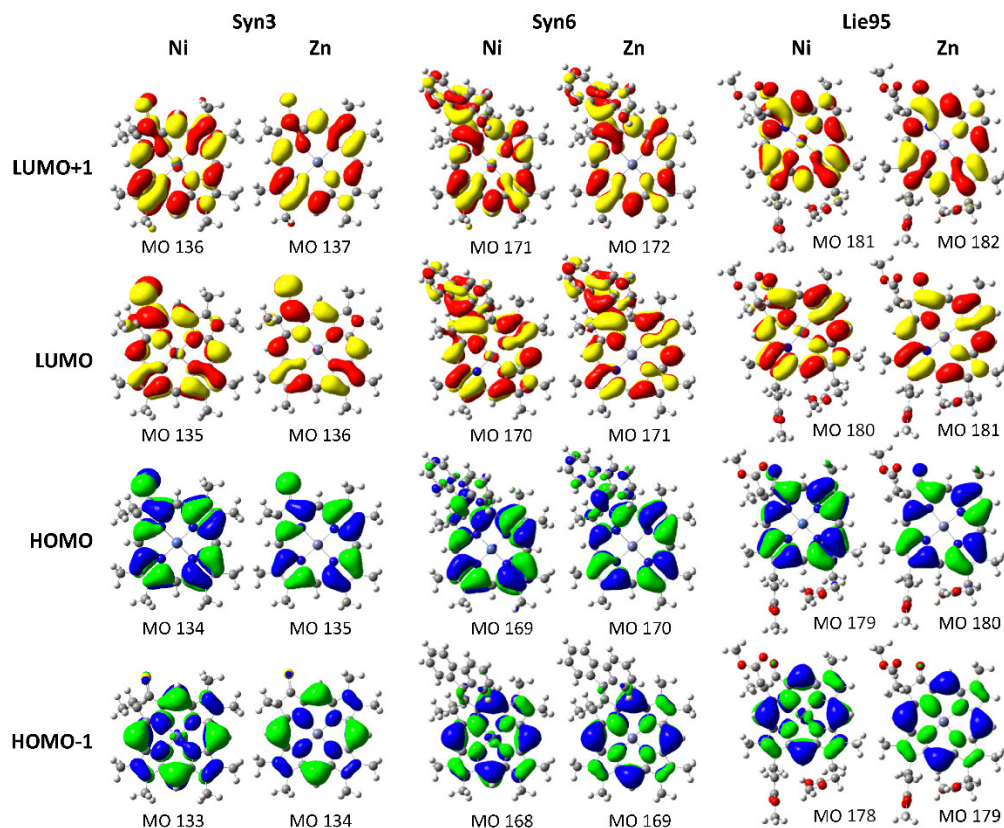
Figure 5-4 The electron density surfaces of the four MOs for Ni- and Zn-coordinated Syn3, Syn6, and Lie95.

5.2.1.4   Influence of β-Substitution and Metal on the Gouterman MOs

For all three chlorins, the a_{1u} orbital lie above the a_{2u} (Figure 5-4). The β-substituents are observed to contribute density in the HOMO (a_{1u}), LUMO, and LUMO+1, with the most density in the LUMO and least density in the HOMO. The presence of electron density on the substituents in the LUMO will help facilitate electron transfer to the CB of the semiconductor.[64] The β-substituents do not contribute density to the a_{2u} orbital (HOMO-1) as a node passes through them. Active β-substituents will connect to the ring π system but the energy of the substituent itself cannot be too high or it will be unable to interact with the ring orbitals. For example, the carbonyl group in **Lie95** does not contribute as much electron density as the thioketone group in **Syn3** because the lower energy sulfur matches the energy of the ring better. The optimized ring geometry for the Ni- and Zn-coordinated chlorins are saddle shaped and planar, respectively.

5.2.2   Fictive Chlorins with Thiophene Substituents

While the synthetic chlorins described above exhibit intense and red-shifted Q bands, the electron transfer component requires additional features. Strong connection between the dye and the semiconductor is necessary for efficient electron transfer.[65] Typically, thiophene units have been used as electron conductors based on their extended π-conjugation.[66, 67] Connection to the CB of TiO_2 is most commonly achieved *via* the carboxylate group. The fluorene in **Syn6** provides a good attachment position for the thiophene units so the base structure of **Syn6** was used to design two fictive chlorins, **M1** and **M2**, with thiophene substituents (Figure 5-5A). The thiophene moiety from Yamamoto *et al.* was utilized.[29]

In **M1**, thiophene units were attached to the fluorene group. In **M2**, thiophene units were attached to the fluorene group and in addition, an electron donating methoxy-substituted triphenylamine was fused to the opposite pyrrole. Zn^{2+} was chosen as the central metal because the presence of the low energy charge transfer and d-d transitions with Ni^{2+} identified in the calculations prevent electron transfer to the CB of TiO_2. These low energy states quench the emission of Ni^{2+} coordinated compounds.
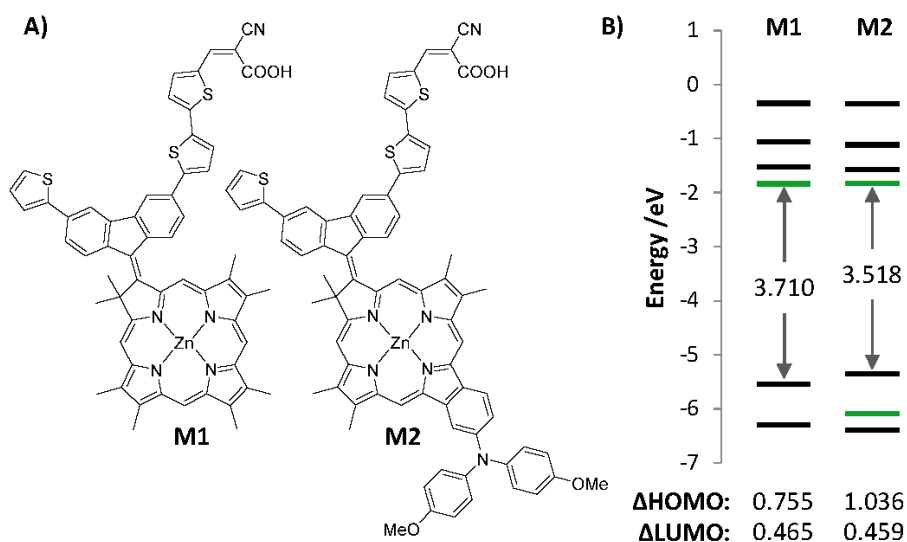

Figure 5-5 (A) Structure of M1 and M2. (B) The energies of the frontier MOs. Substituent-based MOs are highlighted in green (MO 258 for **M1** and MO 323, 321 for **M2**).

5.2.2.1 Electronic Structure of the Fictive Chlorins

M1 and **M2** were designed to exploit the extended π-conjugation at the β-position in chlorins for efficient electron transfer to the CB. The extent of conjugation influences the relative energy of the π MOs. Additional π conjugation results in more orbitals, stabilizing the LUMO and destabilizing the HOMO, which together, reduces the HOMO-LUMO gap and results in a lower energy Q band. In **M1** and **M2**, the presence of the thiophene and donor groups result in this effect. Figure 5-5B shows the energies of the frontier MOs. The most significant change introduced by the thiophene is shown in the analysis of the electron density surfaces (Figure 5-6). In **M1** and **M2**, the LUMO is thiophene-based, rather than the Gouterman LUMO. The Gouterman MOs are identified by their nodal patterns of four for the HOMO pair and five for the LUMO pair. Similar effects of the thiophene on the MO density surfaces have been previously reported.[68, 69] The fusing of an electron donor group on the opposite pyrrole in **M2** introduces a donor-based MO between the typical Gouterman HOMO and HOMO-1 (shown in green in Figure 5-5B). As expected, the donor group added electron density onto the ring and destabilized the HOMO of **M2** when compared with **M1**, resulting in a larger ΔHOMO and smaller HOMO-LUMO gap. The energy of the unoccupied orbitals remained the same.
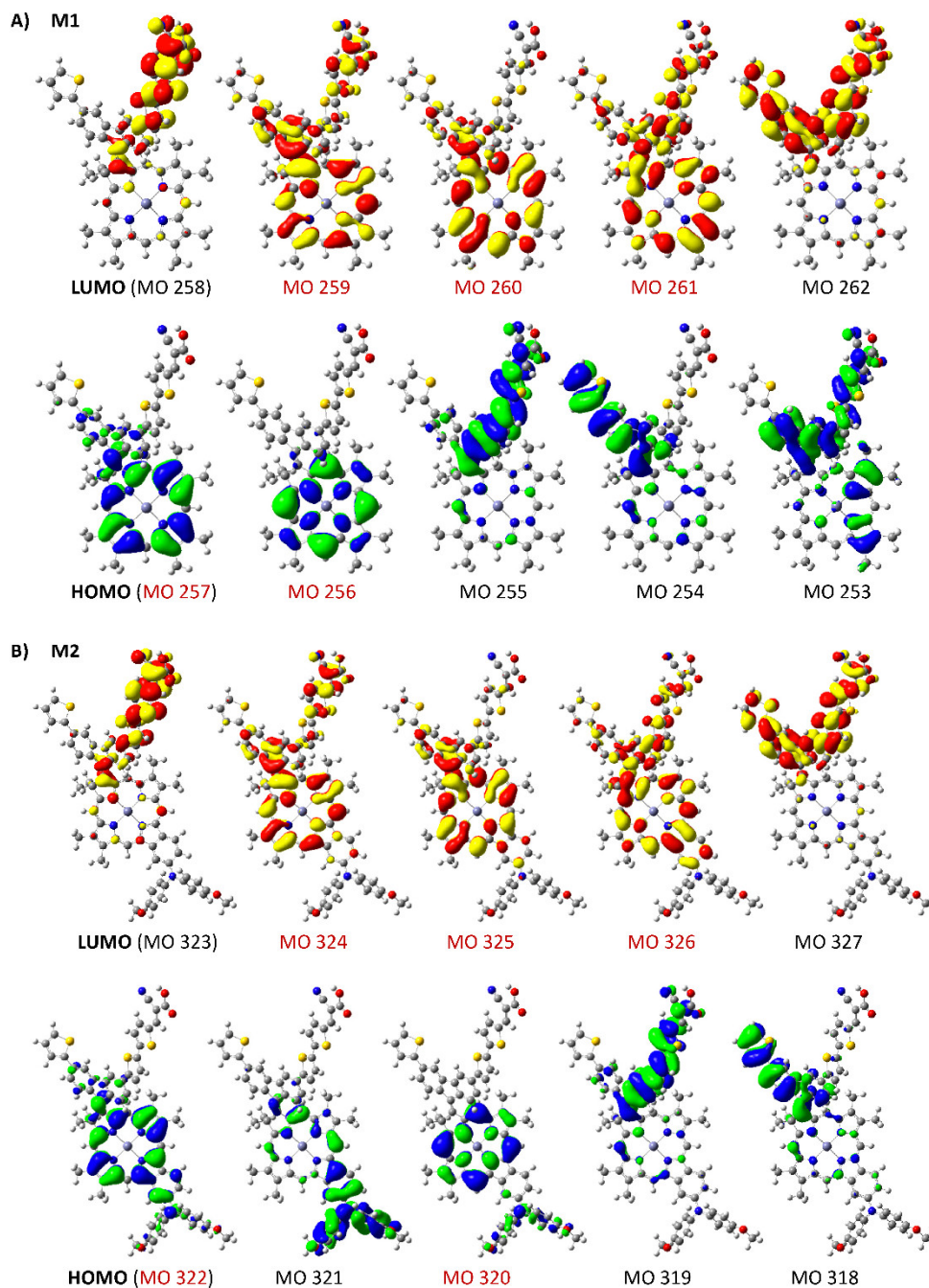
A) M1

LUMO (MO 258)   MO 259   MO 260   MO 261   MO 262

HOMO (MO 257)   MO 256   MO 255   MO 254   MO 253

B) M2

LUMO (MO 323)   MO 324   MO 325   MO 326   MO 327

HOMO (MO 322)   MO 321   MO 320   MO 319   MO 318

Figure 5-6 The electron density surfaces of the frontier MOs for M1 and M2. Gouterman MOs, identified by four nodes for the occupied MOs and five nodes for the unoccupied MOs are highlighted in red. Surfaces are shown with an isovalue of 0.02.

5.2.2.2 Impact of Thiophene and Donor group on the Electronic Structure

For **M1** and **M2**, the thiophene units altered the typical arrangement of the four Gouterman MOs. A thiophene-based MO is introduced below the usual Gouterman LUMO. This means that the thiophene-based MO becomes the LUMO in **M1** (MO 258) and **M2** (MO 323). In addition, three unoccupied MOs with 5 nodes are observed next before the second thiophene-based MO (MO 262 for **M1** and MO 327 for **M2**).

With reference to the electron density surfaces (Figure 5-6), the reason that there are three Gouterman type unoccupied MOs with 5 nodes is due to the presence of the thiophene groups conjugated to the fluorene. Looking at unoccupied MOs of **M1** first, (i) MO 258 (LUMO) involves mainly the thiophene unit on the right side of the fluorene group. Changing the surface isovalue to 0.01 showed the presence of lower electron density on the ring (Appendix D), (ii) MO 259 consists of both left and right thiophene components conjugated over the entire ring, (iii) MO 260 consists primarily of the left fluorene conjugated over the ring, (iv) MO 261 involves mainly the right thiophene conjugated over the ring, and finally above the three π ring MOs, (v) MO 262 involves the entire thiophene group with no conjugation into the ring, like MO 258. Turning now to **M2**, the same electron density pattern is observed from MO 323 to 327, indicating that the presence of the electron donor group does not result in major changes to the unoccupied MOs.

In contrast to the similarity of the electron density distribution in the unoccupied MOs, the highest two occupied MOs for **M1** and **M2** are different because the electron donor MOs are involved. In **M1**, the typical tetrapyrrole a_{1u} and a_{2u} like MOs (MO 256, 257) are observed as the highest occupied. The three relatively isolated thiophene MOs are located just below these two highest occupied MOs (MO 255, 254, 253). In **M2**, however, the a_{1u} like MO is the highest occupied but below this is the conjugated electron donor MO (MO 321). The a_{2u} orbital lies next, and below this orbital are the thiophene-based MOs (MO 317 to 319). It is apparent that the energy of the electron donor has significant influence on the electronic structure of **M2**. As mentioned above, the donor group destabilizes the HOMO (322), thus raising its energy.

The presence of electron density on the thiophene facilitates the charge transfer process to the conduction band. The additional presence of the donor group in **M2** introduces a dipole within the HOMO and LUMO which will further enhance electron transfer to the semiconductor.

5.2.2.3   Spectral Properties of the Fictive Chlorins

The addition of thiophene groups on the fluorene group of **Syn6** extended the π conjugation of the ring, reducing the HOMO–LUMO gap. The resulting Q band energy of **M1** and **M2** (Figure 5-7) are more red-shifted than the Q band of **Syn6**. Attachment of the electron donor group in **M2** further red-shifted the Q band to the computed value of 677 nm. Table 5-4 shows the electronic transitions that give rise to the Q_x and Q_y states of the two thiophene-substituted fictive chlorins. The lower and higher energy states are labeled as Q_{-1} and Q_{+1}, respectively. A significant feature is that the Q states arise from transitions between six MOs for **M1** and seven MOs for **M2**, which is unlike typical tetrapyrroles where the Q band arises solely from transitions between the four Gouterman MOs. In addition, similar to the three synthetic chlorins, multiple bands are observed in the B region, where it is characterized as a panchromatic property of the molecules.

Unlike normal tetrapyrroles where the Q band arises from transitions between the accidentally degenerate HOMOs (a_{1u}, a_{2u}) and the degenerate LUMOs, the Q bands of **M1** and **M2** arise from transitions between HOMO (a_{1u}), HOMO-1 (a_{2u}) into the thiophene-based MO (MO 258 for **M1** and MO 323 for **M2**) and the three unoccupied chlorin ring MOs (MO 259, 260, 261 for **M1** and MO 324, 325, 326 for **M2**).
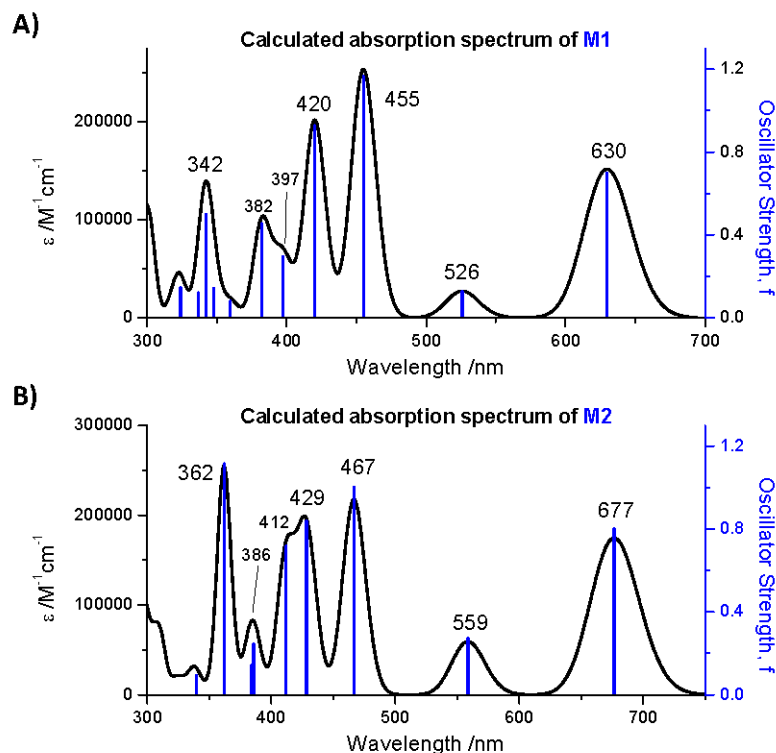
Figure 5-7 The theoretical absorption spectra of (A) M1 and (B) M2 from CAM-B3LYP/6-31G(d,p) TD-DFT calculations.

Table 5-4 Calculated molecular orbital transitions that give rise to the Q bands of M1 and M2. Substituent-based MOs are highlighted in red.

Compound	State	State Energy /nm	f	Transition (contribution)
M1	Q$_{-1}$	629.79	0.6978	256→260 (7%)
				257→258 (20%)
				257→259 (67%)
	Q$_{+1}$	525.86	0.1255	256→258 (4%)
				256→259 (22%)
				256→261 (3%)
				257→258 (4%)
				257→260 (61%)
				257→261 (2%)
M2	Q$_{-1}$	676.72	0.8027	320→325 (5%)
				322→323 (24%)
				322→324 (63%)
	Q$_{+1}$	558.72	0.2730	320→323 (3%)
				320→324 (12%)
				321→324 (3%)
				322→323 (4%)
				322→325 (67%)
				322→326 (3%)

5.2.2.4   Energy Level Alignment for Efficient Dye Sensitization

The PCE of DSSCs depends on efficient electron transfer from the dye's excited state to the TiO_2 conduction band and fast regeneration of the oxidized dye by the redox couple (I^-/I_3^-).[70] The ground state oxidation potential (GSOP) and the excited state oxidation potential (ESOP) provide a quantitative estimate of the efficiency of the electron transfer and regeneration. The ESOP of the dye should lie above the TiO_2 conduction band and the GSOP of the dye should lie below the redox mediator (I^-/I_3^-) by at least 0.2 eV for both.[71] According to Koopman's Theorem, the GSOP could be approximated by the HOMO energy of the neutral species. The ESOP can then be approximated by adding the energy of the lowest excited state, E_{0-0}, to the GSOP (in this case, the energy of the HOMO).[72, 73] The E_{0-0} can be obtained from the optical spectrum as the lowest energy absorption band and can also be approximated by the first excited state from TD-DFT calculations. The TiO_2 conduction band energy and I^-/I_3^- redox couple potential used here are -4.0 eV and -4.8 eV, respectively.[74]
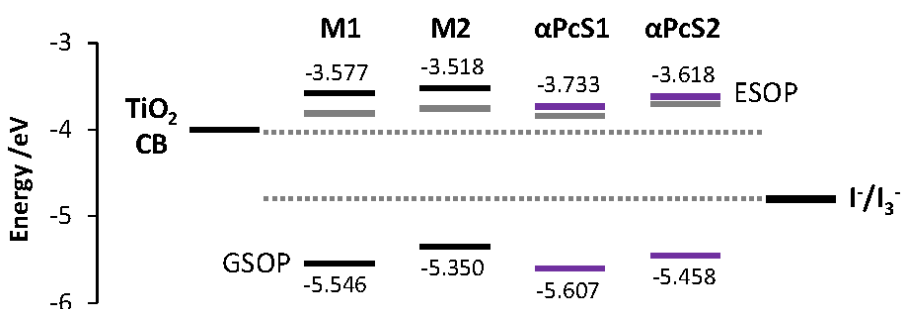
Figure 5-8 The GSOP and ESOP values of M1, M2, αPcS1, and αPcS2 with respect to the energies of the TiO₂ conduction band (-4.0 eV) and I⁻/I₃⁻ redox potential (-4.8 eV). Grey lines show the ESOP value calculated using the experimental Q band energy. Their values are -3.81, -3.75, -3.84, and -3.71 eV for **M1, M2, αPcS1,** and **αPcS2**, respectively.

Figure 5-8 shows the values of GSOP and ESOP for **M1**, **M2**, **αPcS1**, and **αPcS2** with respect to the TiO_2 conduction band energy and I^-/I_3^- redox couple potential. **αPcS1**, and **αPcS2** are previously studied phthalocyanines with a PCE of 5.5% and 3.8%, respectively, that involved thiophene substituents.[29] The black/purple lines shown in Figure 5-8 follow

the procedures of using the HOMO energy and the calculated excited state energy from a single TD-DF calculation to obtain the values for GSOP and ESOP. Both the GSOP and ESOP of **M1** and **M2** align well with the CB and redox potential, suggesting efficient electron transfer and dye regeneration. The GSOPs of **M1** and **M2** were about 0.74 eV and 0.55 eV lower from the redox couple, respectively. The closer GSOP of **M2** to the redox couple would make dye regeneration faster and possibly more efficient than **M1**. Fast reduction of the oxidized dye will reduce recombination from the first excited state back onto the ground state. The calculated ESOPs of **M1** and **M2** were above the CB by about 0.45 eV. The ESOP magnitudes can be adjusted using the estimated experimental value of the excited state energy of **M1** and **M2** from the trend in Figure 5-9C (grey lines in Figure 5-8). As expected, the experimental ESOP is lower in energy than the calculated ESOP, since TD-DFT overestimates the energy of the first excited state.

5.2.3   Connecting Experimental Data with Computational Results

An updated version of the trends reported in 2005, using the CAM-B3LYP functional, was used again to help connect the experimental Q bands with computationally derived data.[19] These trends provide a connection between each molecule's electronic structure and its respective spectroscopic properties. The trends showed that the energy of the Q bands is proportional to the HOMO-LUMO gap and the intensity of the Q bands (oscillator strength) is proportional to the magnitude of ΔHOMO.

In Figure 5-9A, the observed Q band energy is plotted as a function of the HOMO-LUMO gap for a set of extended π conjugated porphyrins and phthalocyanines, together with the data for the three synthetic chlorins and the predicted Q band energies of **M1** and **M2**. The data for **M1** and **M2** are extracted from the trend in Figure 5-9C. Although **Syn3**, **Syn6**, **Lie95**, **M1**, and **M2** are chlorins, their data lie closely around the trend line in Figure 5-9A. The magnitude of the HOMO-LUMO gap is dependent on the functional used, but the state energy should remain the same regardless of the functional used. The fact that the Q band energy is linear with the HOMO-LUMO gap indicates that the HOMO to LUMO transition dominates the first excited state, as predicted by the Gouterman model. It is significant that the experimental Q band energy can be predicted regardless of the kind of tetrapyrrole involved. The substitution of thioketone (**Syn3**) and fluorene (**Syn6**) at the β-position of

the chlorin stabilized the LUMO, resulting in a smaller HOMO-LUMO gap than Chl *a*, red-shifting the Q band. The addition of thiophene units in the fictive chlorins stabilized the LUMO further and the extra donating group in **M2** destabilized the HOMO. The significantly red-shifted Q band and the presence of thiophene-based MOs between the Gouterman MOs make **M2** a good dye candidate for DSSCs.

Figure 5-9B shows the computationally derived oscillator strengths for the set of porphyrins and phthalocyanines together with the data for the three synthetic chlorins and **M1** and **M2**. The three synthetic chlorins and Chl *a* lie around the trend line. On the other hand, the oscillator strengths of **M1** and **M2** lie well of the trend line, with Q band intensity much higher than the phthalocyanines (Pc, Nc, $\alpha(C_6H_5)_8Pc$) but with much smaller magnitude of ΔHOMO. This unusual relationship is likely a result of the transition complexity of the first excited state that comprises transitions between MOs that are not the ring π MOs.

Figure 5-9C shows the experimental Q band wavelength as a function of the calculated Q band wavelength for a set of chlorins previously synthesized and reported by Montforts, **7-10** (Appendix E),[37, 75] along with the chlorins described in this chapter. Although TD-DFT calculations overestimate the energy of the first excited state, which is responsible for the Q band, the linear trend line shows that this error is systematic. Using the trend line, the predicted experimental Q band wavelengths for the fictive chlorins, **M1** and **M2**, were estimated to be 716 and 777 nm, respectively. These estimated experimental Q band energies were used to plot **M1** and **M2** in Figure 5-9A. The effect of the combined electron donor and acceptor substituents greatly red-shifts and intensifies the Q band in **M2**.
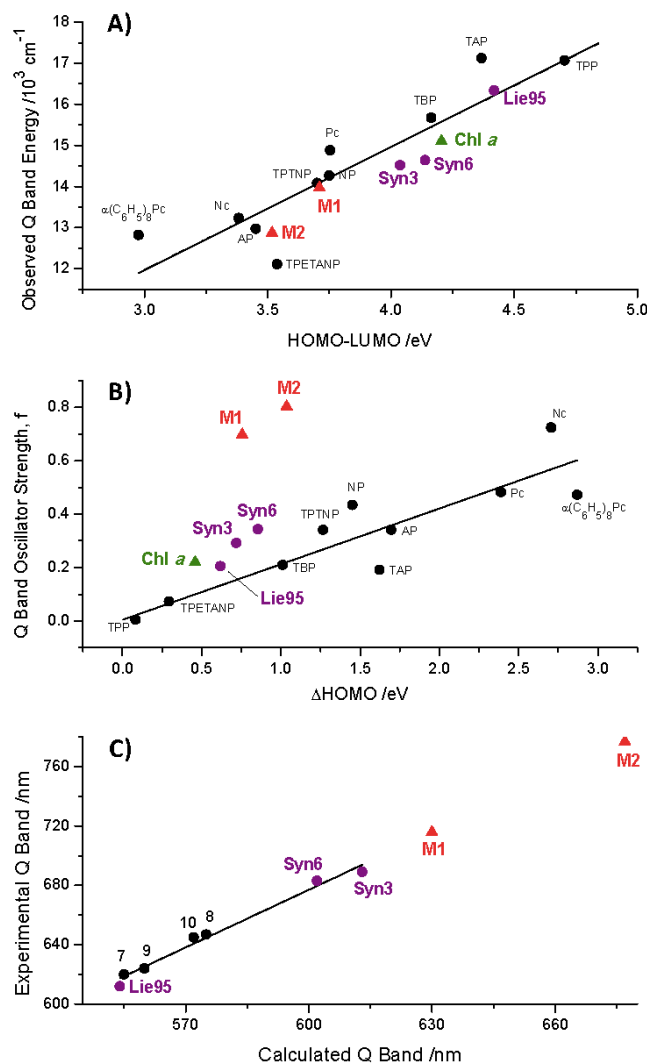
Figure 5-9 (A) Observed Q band energy *versus* the calculated HOMO-LUMO gap. (B) The oscillator strength, *f*, of the Q band *versus* the calculated ΔHOMO. (C) The experimental Q band wavelength *versus* the theoretical Q band wavelength. Compounds **7**-**10** were previously synthesized chlorins by Montforts.

5.3   Conclusions

Three Ni-coordinated synthetic chlorins with β-substitution of thioketone (**Syn3**), fluorene (**Syn6**), and ketone (**Lie95**) were studied using MCD spectroscopy and DFT methods for potential application as dyes for DSSCs. Calculations were also performed on Zn-coordinated **Syn3**, **Syn6**, and **Lie95** to identify Ni-dependent optical bands. Although the Zn- and Ni-coordinated chlorins exhibited similar theoretical absorption spectra, the

unfilled d-orbitals of the Ni^{2+} introduced charge transfer and d-d transitions in addition to the typical transitions between the Gouterman MOs. Depending on the nature of the electron withdrawing or electron donating properties of the β-substituents, the Gouterman MOs are stabilized or destabilized, respectively. The three substituents in these chlorins were all electron withdrawing and as a result, both occupied and unoccupied MOs were lower in energy than the unsubstituted chlorin. In addition, the substituents reduced the HOMO-LUMO gap, resulting in red-shifts of the Q band.

While the three synthetic chlorins showed the intense and red Q bands required for dye sensitization in DSSCs, they lack an anchor that will connect them to the semiconductor. Of the three chlorins, the fluorene group in **Syn6** offered a connection site for the thiophene units. Based on the structure of **Syn6**, **M1** was designed with just the thiophene attached to the fluorene while **M2** included a thiophene and a donor group on the opposite pyrrole. The substitution with the thiophene units introduced a thiophene-based MO between the typical Gouterman HOMO and LUMO and generated three unoccupied ring π MOs (eg. MO 259, 260, and 261 for **M1**) instead of the usual two. The additional donor group in **M2** introduced a donor-based MO between the usual Gouterman HOMO and HOMO-1. The electron donating effect of the donor group destabilized the HOMO and brought it closer to the LUMO. Despite the relatively small ΔHOMO, **M1** and **M2** exhibited a very intense Q band. The panchromatic absorption observed from the theoretical absorption spectra, the intense and red-shifted Q band, and the presence of the donor- and thiophene-based MO properties of **M2** make it a possible candidate for application in DSSCs.

Chapter 6

6   Summary

This study showed that computational methods can be used to both understand the spectroscopic data of known tetrapyrroles and guide the design of novel synthetic tetrapyrroles for solar cell applications. The experimental data from previously synthesized tetrapyrroles were key to the calibration of the computational parameters. This allows the reliable prediction of properties for fictive molecule designs before actual synthesis.
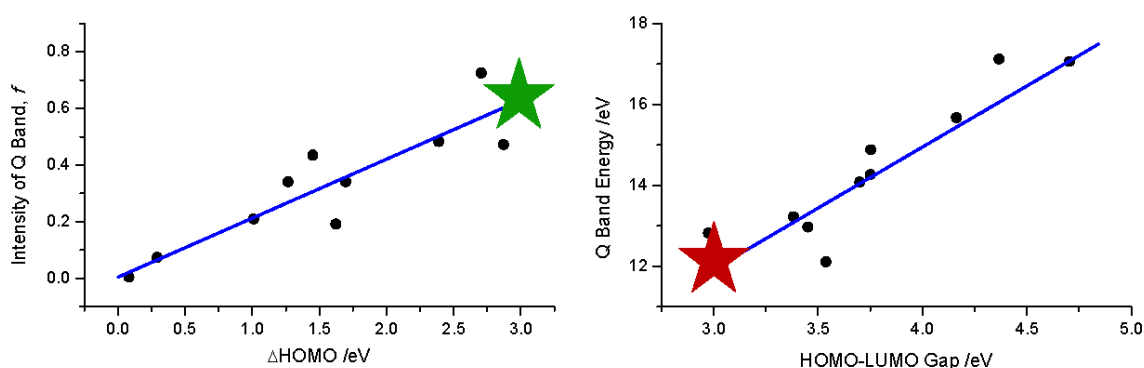
Figure 6-1 Trends connecting the Q band intensity and energy with the computed electronic structure. The green and red stars show where an ideal dye for DSSCs would lie on the trend.

Figure 6-1 summarises the ideal spectroscopic properties for tetrapyrrole design for DSSC applications that were described in this thesis: an intense Q band and a red Q band (700-900 nm). The highly absorbing Q band and a lower energy Q band (or first excited state) leads to more efficient electron transfer to the semiconductor. The intensity of the Q band is proportional to the magnitude of splitting between the nominally degenerate Gouterman HOMO pair while the energy of the Q band is proportional to the HOMO-LUMO gap. The experimental data used in the original trends[19] imply that there is a limit to the extent of the splitting of the HOMO pair. Therefore, it is important to find ways of splitting the LUMO pair as well, in order to further decrease the HOMO-LUMO gap. The chlorophyll data in Chapter 3 and fictive porphyrin data in Chapter 4 showed that the splitting of the LUMO pair can be achieved by using a combination of the chlorin ring, strong electron withdrawing groups on the 2/3 β-positions, and extended π-conjugation.
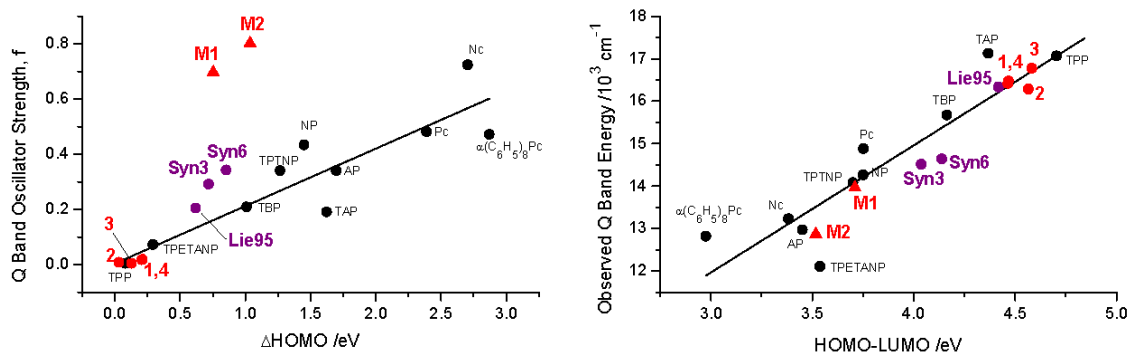
Figure 6-2 Summary trend plots with the data of synthetic porphyrins (1-4, Chapter 4), synthetic chlorins (Syn3, Syn6, Lie95, Chapter5), and fictive chlorins (M1 and M2, Chapter 5).

The assessment of the spectroscopic properties of the porphyrins in Chapter 4 and chlorins in Chapter 5 (Figure 6-2) with respect to application as dyes show that they do not exhibit the ideal properties illustrated in Figure 6-1. However, the design of the fictive molecules in Chapter 5, **M1** and **M2**, overcame the limitations of the synthetic tetrapyrroles, resulting in unique Q bands that were red-shifted and more intense than phthalocyanines while exhibiting a relatively small ΔHOMO. Phthalocyanines are known to have large values of ΔHOMO due to the nitrogen atoms at the *meso*-position, which selectively affects the a_{2u} orbital more than the a_{1u} orbital. Although phthalocyanines exhibit intense Q bands, they are often poorly soluble, aggregate easily, and are expensive to make and purify. Therefore, computationally guided design of **M1** and **M2** has provided a synthetic route to tetrapyrroles with intense Q bands without the need for *meso*-nitrogen atoms.

References

1.   L. R. Milgrom, *The Colours of Life: An Introduction to the Chemistry of Porphyrins and Related Compounds*, Oxford University Press, New York, 1997.
2.   T. Tanaka and A. Osuka, *Chem. Soc. Rev.*, 2015, **44**, 943-969.
3.   T. Higashino and H. Imahori, *Dalton Trans.*, 2015, **44**, 448-463.
4.   H. Imahori, K. Kurotobi and M. G. Walter, in *Handbook of Porphyrin Science*, eds. K. M. Kadish, K. M. Smith and R. Guilard, World Scientific Publishing, Singapore, 2012, vol. 18, ch. 80, pp. 57-121.
5.   M. Ethirajan, Y. Chen, P. Joshi and R. K. Pandey, *Chem. Soc. Rev.*, 2011, **40**, 340-362.
6.   R. Bonnett, in *The Porphyrins*, ed. D. Dolphin, Academic Press, New York, 1978, vol. 1, p. 1.
7.   J. E. Merritt and K. L. Loening, *Eur. J. Biochem.*, 1980, **108**, 1-30.
8.   M. J. Stillman, in *Handbook of Porphyrin Science*, eds. K. M. Kadish, K. M. Smith and R. Guilard, World Scientific Publishing, Singapore, 2011, vol. 14, ch. 65, pp. 461-524.
9.   M. T. Tiedemann and M. J. Stillman, *J. Porphyrins Phthalocyanines*, 2011, **15**, 1134-1149.
10.   A. Zhang and M. J. Stillman, *Phys. Chem. Chem. Phys.*, 2018, **20**, 12470-12482.
11.   M. Taniguchi, M. Ptaszek, B. E. McDowell, P. D. Boyle and J. S. Lindsey, *Tetrahedron*, 2007, **63**, 3850-3863.
12.   H. L. Kee, C. Kirmaier, Q. Tang, J. R. Diers, C. Muthiah, M. Taniguchi, J. K. Laha, M. Ptaszek, J. S. Lindsey, D. F. Bocian and D. Holten, *Photochem. Photobiol.*, 2007, **83**, 1125-1143.
13.   M. Gouterman, *J. Chem. Phys.*, 1959, **30**, 1139-1161.
14.   M. Gouterman, *J. Mol. Spectrosc.*, 1961, **6**, 138-163.
15.   M. Gouterman, in *The Porphyrins*, ed. D. Dolphin, Academic Press, New York, 1978, vol. 3, ch. 1, pp. 1-165.
16.   M. Fragata, B. Nordén and T. Kurucsev, *Photochem. Photobiol.*, 1988, **47**, 133-143.
17.   C. Weiss, *Ann. N. Y. Acad. Sci.*, 1975, **244**, 204-213.
18.   T. Nyokong, Z. Gasyna and M. J. Stillman, *Inorg. Chem.*, 1987, **26**, 1087-1095.
19.   J. Mack, Y. Asano, N. Kobayashi and M. J. Stillman, *J. Am. Chem. Soc.*, 2005, **127**, 17697-17711.
20.   J. Mack and M. J. Stillman, in *The Porphyrin Handbook*, eds. K. M. Kadish, K. M. Smith and R. Guilard, Academic Press, New York, 2003, vol. 16, ch. 103, pp. 43-116.
21.   J. Mack, M. J. Stillman and N. Kobayashi, *Coord. Chem. Rev.*, 2007, **251**, 429-453.
22.   A. Zhang, L. Kwan and M. J. Stillman, *Org. Biomol. Chem.*, 2017, **15**, 9081-9094.
23.   B. O'Regan and M. Grätzel, *Nature*, 1991, **353**, 737-740.
24.   S. Mathew, A. Yella, P. Gao, R. Humphry-Baker, B. F. Curchod, N. Ashari-Astani, I. Tavernelli, U. Rothlisberger, M. K. Nazeeruddin and M. Gratzel, *Nat. Chem.*, 2014, **6**, 242-247.

25. M. A. Green, K. Emery, Y. Hishikawa, W. Warta and E. D. Dunlop, *Prog. Photovolt: Res. Appl.*, 2015, **23**, 1-9.
26. M. Grätzel, *Nature*, 2001, **414**, 338-344.
27. M. Grätzel, *J. Photochem. Photobiol. C.*, 2003, **4**, 145-153.
28. B. E. Hardin, H. J. Snaith and M. D. McGehee, *Nature Photonics*, 2012, **6**, 162-169.
29. S. Yamamoto, A. Zhang, M. J. Stillman, N. Kobayashi and M. Kimura, *Chem. Eur. J.*, 2016, **22**, 18760-18768.
30. D. L. Wong, A. Zhang, A. S. Faponle, S. P. de Visser and M. J. Stillman, *Metallomics*, 2017, **9**, 501-516.
31. R. Zhang, P. Chauhan, D. Tao, A. Zhang, M. J. Stillman, N. Yan and Z. Ding, unpublished work.
32. A. M. Polgar, F. Weigend, A. Zhang, M. J. Stillman and J. F. Corrigan, *J. Am. Chem. Soc.*, 2017, **139**, 14045-14048.
33. A. M. Polgar, A. Zhang, M. J. Stillman and J. F. Corrigan, unpublished work.
34. R. H. E. Hudson, in *Chemistry 2273a September 2010 Laboratory Manual*, The University of Western Ontario, London, ON, 2010, p. 26.
35. R. G. W. Jinadasa, Y. Fang, Y. Deng, R. Deshpande, X. Jiang, K. M. Kadish and H. Wang, *RSC Adv.*, 2015, **5**, 51489-51492.
36. F. Dullweber and F.-P. Montforts, *Synlett*, 2008, **2008**, 3213-3215.
37. J. W. Bats, G. Haake, A. Meier, F.-P. Montforts and G. Scheurich, *Liebigs Ann.*, 1995, **1995**, 1617-1631.
38. J. Linnanto and J. Korppi-Tommola, *J. Comput. Chem.*, 2004, **25**, 123-137.
39. Gaussian 09, Revision E.01, M. J. Frisch, G. W. Trucks, H. B. Schlegel, G. E. Scuseria, M. A. Robb, J. R. Cheeseman, G. Scalmani, V. Barone, B. Mennucci, G. A. Petersson, H. Nakatsuji, M. Caricato, X. Li, H. P. Hratchian, A. F. Izmaylov, J. Bloino, G. Zheng, J. L. Sonnenberg, M. Hada, M. Ehara, K. Toyota, R. Fukuda, J. Hasegawa, M. Ishida, T. Nakajima, Y. Honda, O. Kitao, H. Nakai, T. Vreven, J. A. Montgomery, Jr., J. E. Peralta, F. Ogliaro, M. Bearpark, J. J. Heyd, E. Brothers, K. N. Kudin, V. N. Staroverov, T. Keith, R. Kobayashi, J. Normand, K. Raghavachari, A. Rendell, J. C. Burant, S. S. Iyengar, J. Tomasi, M. Cossi, N. Rega, J. M. Millam, M. Klene, J. E. Knox, J. B. Cross, V. Bakken, C. Adamo, J. Jaramillo, R. Gomperts, R. E. Stratmann, O. Yazyev, A. J. Austin, R. Cammi, C. Pomelli, J. W. Ochterski, R. L. Martin, K. Morokuma, V. G. Zakrzewski, G. A. Voth, P. Salvador, J. J. Dannenberg, S. Dapprich, A. D. Daniels, O. Farkas, J. B. Foresman, J. V. Ortiz, J. Cioslowski, and D. J. Fox, Gaussian, Inc., Wallingford CT, 2013.
40. A. Tomberg, *Gaussian 09W Tutorial*, n.d.
41. Z.-L. Cai, M. J. Crossley, J. R. Reimers, R. Kobayashi and R. D. Amos, *J. Phys. Chem. B*, 2006, **110**, 15624-15632.
42. A. Kay and M. Gratzel, *J. Phys. Chem.*, 1993, **97**, 6272-6277.
43. M. Chen and R. E. Blankenship, *Trends Plant Sci.*, 2011, **16**, 427-431.
44. J. M. Yuen, M. A. Harris, M. Liu, J. R. Diers, C. Kirmaier, D. F. Bocian, J. S. Lindsey and D. Holten, *Photochem. Photobiol.*, 2015, **91**, 331-342.
45. D. Frackowiak, D. Bauman, H. Manikowski, W. R. Browett and M. J. Stillman, *Biophys. Chem.*, 1987, **28**, 101-114.

46. C. Weiss, *J. Mol. Spectrosc.*, 1972, **44**, 37-80.
47. H. Ozawa, T. Sugiura, T. Kuroda, K. Nozawa and H. Arakawa, *J. Mater. Chem. A*, 2016, **4**, 1762-1770.
48. R. Croce and H. van Amerongen, *Nat. Chem. Biol.*, 2014, **10**, 492-501.
49. C. A. Tracewell, A. Cua, D. H. Stewart, D. F. Bocian and G. W. Brudvig, *Biochemistry*, 2001, **40**, 193-203.
50. X. F. Wang, O. Kitao, H. Zhou, H. Tamiaki and S. Sasaki, *Chem. Commun.*, 2009, 1523-1525.
51. X.-F. Wang, H. Tamiaki, O. Kitao, T. Ikeuchi and S.-i. Sasaki, *J. Power Sources*, 2013, **242**, 860-864.
52. M. O. Senge and S. A. MacGowan, in *Handbook of Porphyrin Science*, eds. K. M. Kadish, K. M. Smith and R. Guilard, World Scientific Publishing, Singapore, 2011, vol. 13, ch. 61, pp. 253-297.
53. X. F. Wang, H. Tamiaki, L. Wang, N. Tamai, O. Kitao, H. Zhou and S. Sasaki, *Langmuir*, 2010, **26**, 6320-6327.
54. D. Kim and A. Osuka, *J. Phys. Chem. A*, 2003, **107**, 8791-8816.
55. T. Okujima, J. Mack, J. Nakamura, G. Kubheka, T. Nyokong, H. Zhu, N. Komobuchi, N. Ono, H. Yamada, H. Uno and N. Kobayashi, *Chem. Eur. J.*, 2016, **22**, 14730-14738.
56. T. Higashino, Y. Tsuji, Y. Fujimori, K. Sugiura, S. Ito and H. Imahori, *Chem. Lett.*, 2015, **44**, 1395-1397.
57. Y. Liu, N. Xiang, X. Feng, P. Shen, W. Zhou, C. Weng, B. Zhao and S. Tan, *Chem. Commun.*, 2009, 2499-2501.
58. L. L. Li and E. W. Diau, *Chem. Soc. Rev.*, 2013, **42**, 291-304.
59. M. Urbani, M. Gratzel, M. K. Nazeeruddin and T. Torres, *Chem. Rev.*, 2014, **114**, 12330-12396.
60. M. P. Balanay and D. H. Kim, *Phys. Chem. Chem. Phys.*, 2008, **10**, 5121-5127.
61. N. Kobayashi, J. Mack, K. Ishii and M. J. Stillman, *Inorg. Chem.*, 2002, **41**, 5350-5363.
62. V. N. Nemykin, R. G. Hadt, R. V. Belosludov, H. Mizuseki and Y. Kawazoe, *J. Phys. Chem. A*, 2007, **111**, 12901-12913.
63. A. Dreuw and M. Head-Gordon, *J. Am. Chem. Soc.*, 2004, **126**, 4007-4016.
64. N. Santhanamoorthi, C. M. Lo and J. C. Jiang, *J. Phys. Chem. Lett.*, 2013, **4**, 524-530.
65. S. Kim, J. K. Lee, S. O. Kang, J. Ko, J.-H. Yum, S. Fantacci, F. D. Angelis, D. D. Censo, M. K. Nazeeruddin and M. Gratzel, *J. Am. Chem. Soc.*, 2006, **128**, 16701-16707.
66. A. Mishra, N. Pootrakulchote, M. K. Fischer, C. Klein, M. K. Nazeeruddin, S. M. Zakeeruddin, P. Bauerle and M. Gratzel, *Chem. Commun.*, 2009, 7146-7148.
67. M. P. Balanay and D. H. Kim, *J. Phys. Chem. C*, 2011, **115**, 19424-19430.
68. M.-D. Zhang, Z.-Y. Zhang, Z.-Q. Bao, Z.-M. Ju, X.-Y. Wang, H.-G. Zheng, J. Ma and X.-F. Zhou, *J. Mater. Chem. A*, 2014, **2**, 14883-14889.
69. S. J. Lind, K. C. Gordon, S. Gambhir and D. L. Officer, *Phys. Chem. Chem. Phys.*, 2009, **11**, 5598-5607.
70. M. Grätzel, *J. Photoch. Photobio. A*, 2004, **164**, 3-14.
71. A. D. Becke, *J. Chem. Phys.*, 1993, **98**, 5648-5652.

72.   F. De Angelis, S. Fantacci and A. Selloni, *Nanotechnology*, 2008, **19**, 424002.
73.   M. Pastore, S. Fantacci and F. D. Angelis, *J. Phys. Chem. C*, 2010, **114**, 22742-22750.
74.   S. Meng, E. Kaxiras, M. K. Nazeeruddin and M. Grätzel, *J. Phys. Chem. C*, 2011, **115**, 9276-9282.
75.   O. Kutzki and F.-P. Montforts, *Synlett*, 2001, **2001**, 53-56.

Appendices

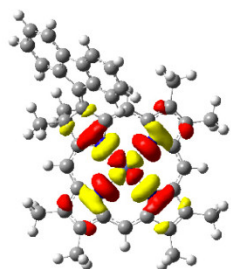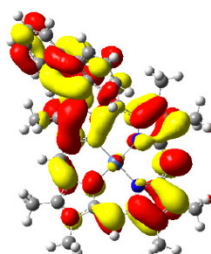**Appendix A: Electron density surfaces for non-Gouterman MOs of Ni-coordinated Syn3.**
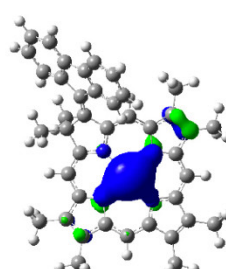
Syn3-Ni
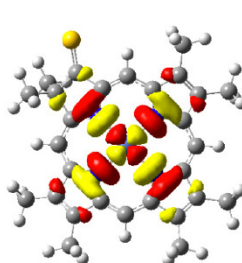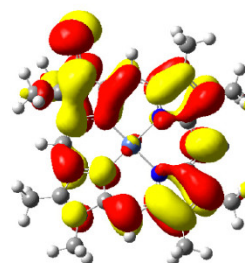
MO 138   MO 137
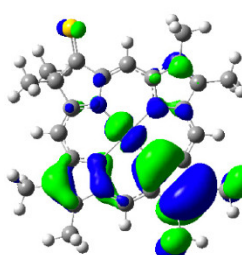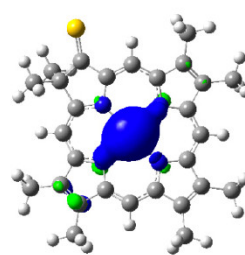
MO 132   MO 130   MO 129
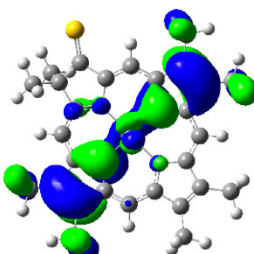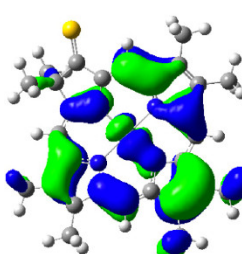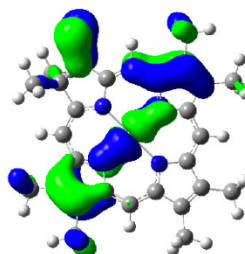
MO 128   MO 126   MO 125
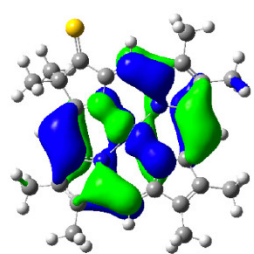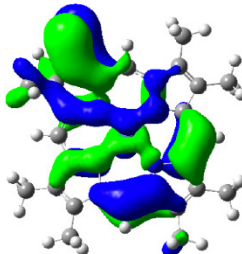
MO 124   MO 123

Appendix B: Electron density surfaces for non-Gouterman MOs of Ni-coordinated Syn6.

Syn6-Ni

MO 174

MO 172
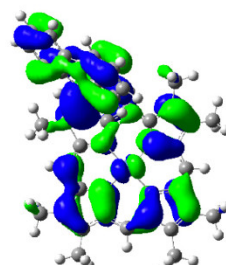
MO 167
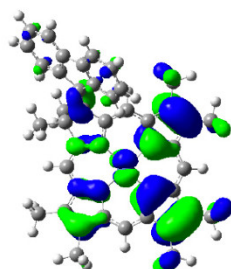
MO 165
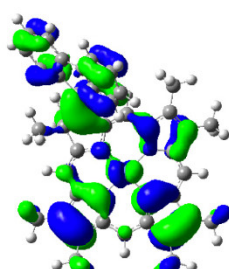
MO 164

MO 163
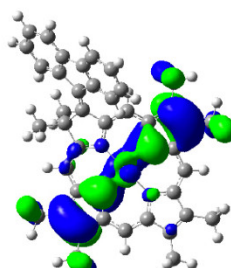
MO 162
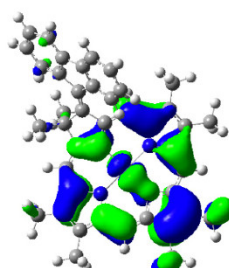
MO 160
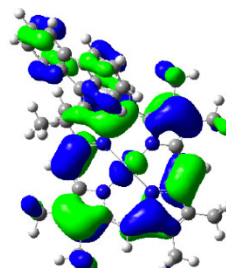
MO 159
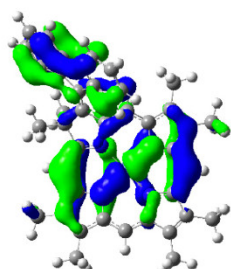
MO 158
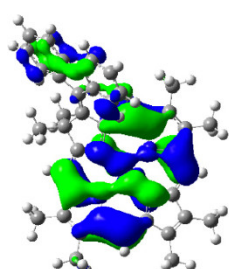
MO 157
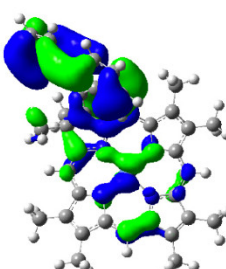
MO 156

Appendix C: Electron density surfaces for non-Gouterman MOs of Ni-coordinated Lie95.

Lie95-Ni

MO 183   MO 182   MO 177

MO 176   MO 175   MO 174

MO 172   MO 171   MO 170

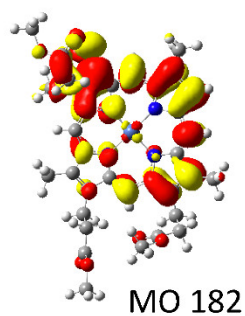MO 169   MO 168   MO 167
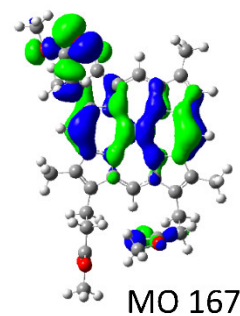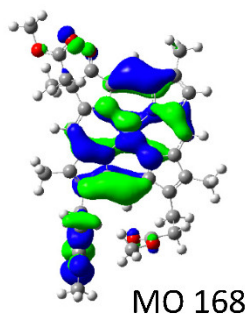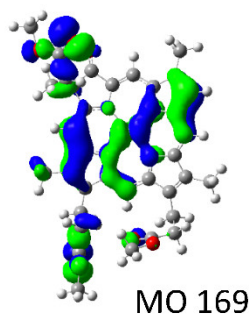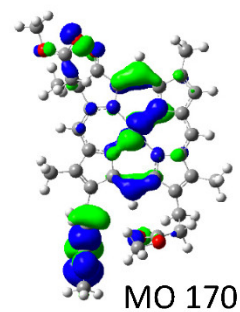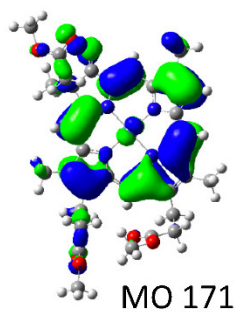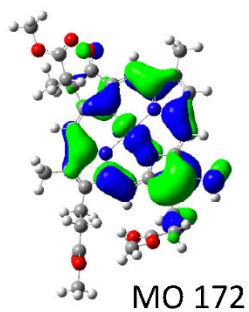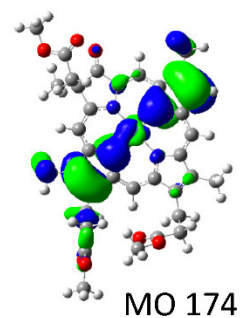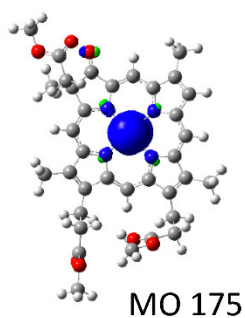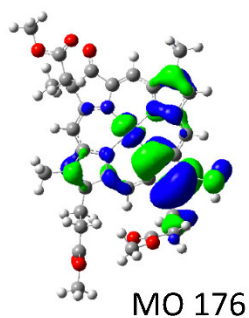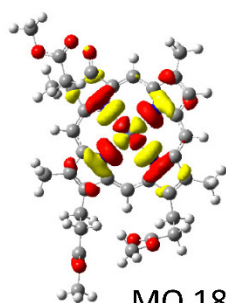
Appendix D: HOMO and LUMO electron density surfaces for M1 with different isovalues.

M1

Isovalue
0.01

0.005

HOMO 256   LUMO 257
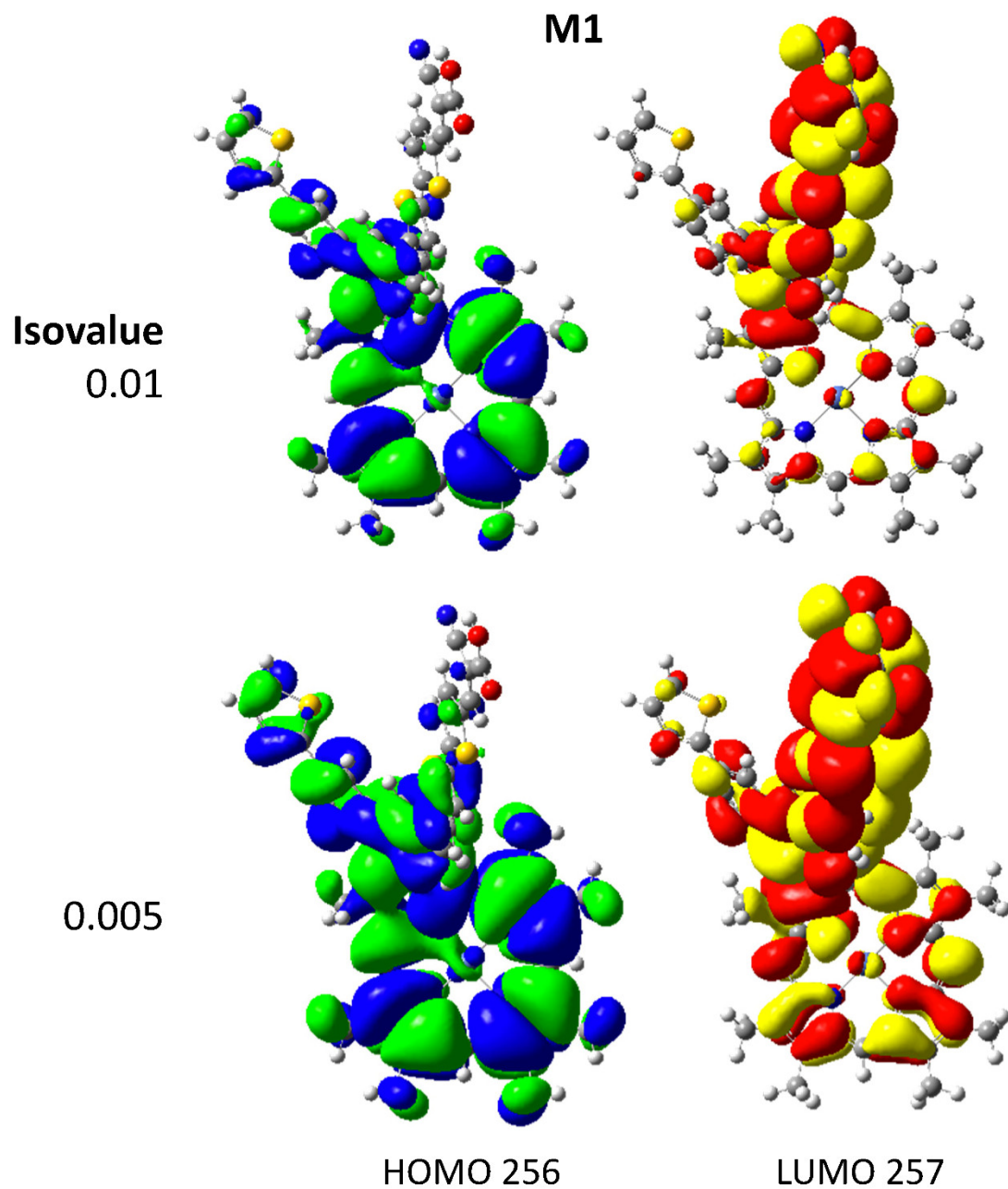
Appendix E: Structures of compounds 7-10, from Montforts *et al.*
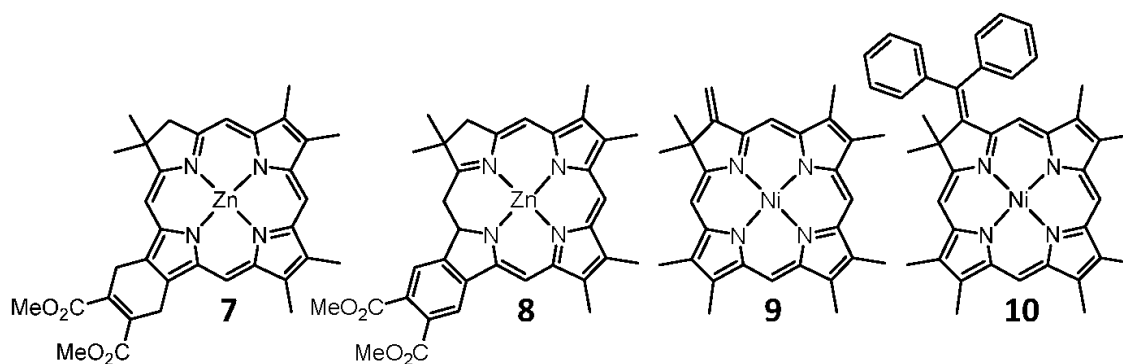
Curriculum Vitae

Name:	Angel (Qi Wen) Zhang
Post-secondary Education and Degrees:	The University of Western Ontario London, Ontario, Canada 2012-2016 B. Sc. Honors Specialization in Chemistry The University of Western Ontario London, Ontario, Canada 2016-Present M. Sc. In Chemistry
Honours and Awards:	Ontario Graduate Scholarship 2017-2018 Graduate School Entrance Award 2016 NSERC Undergraduate Student Research Award 2015 NSERC Undergraduate Student Research Award 2014
Related Work Experience	Laboratory Teaching Assistant 2213A, 2223B The University of Western Ontario 2016-2017 Undergraduate Research Assistant, NSERC USRA The University of Western Ontario, Corrigan Group 2015 Undergraduate Research Assistant, NSERC USRA The University of Western Ontario, Huang Group 2014

Publications:

1. **Zhang, A.**; Stillman, M. J. Computational studies on the spectral and electronic properties of chlorophyll: connection between structure and the split LUMO. **2018**, In preparation.

2. Polgar, A.; **Zhang, A.**; Stillman, M. J.; Corrigan, J. Plug and play: tunable metal/chalcogen composition in copper(I)-chalcogenide self-assemblies enabled by cyclic (alkyl)(amino)carbenes. *J. Am. Chem. Soc.* **2018**, Submitted.

3. **Zhang, A.**; Stillman, M. J. Computational guidance in the design of functional tetrapyrroles. In *Handbook of Porphyrin Science*, Kadish, K. M.; Smith, K. M.; Guilard, R., Eds. **2018**, Under editorial process.

4. **Zhang, A.**; Stillman, M. J. Exploring function activated chlorins using MCD spectroscopy and DFT methods: design of a chlorin with a remarkably intense, red Q band. *Phys. Chem. Chem. Phys.*, **2018**, 20, 12470-12482.

5. Polgar, A. M.; Weigend, F.; **Zhang, A.**; Stillman, M. J.; Corrigan, J. F. A *N*-heterocyclic carbene-stabilized coinage metal-chalcogenide framework with tunable optical properties. *J. Am. Chem. Soc.* **2017**, 139, 14045-14048.

6. **Zhang, A.**; Kwan, L.; Stillman, M. J. The spectroscopic impact of interactions with the four Gouterman orbitals from peripheral decoration of porphyrins with simple electron withdrawing and donating groups. *Org. Biomol. Chem.*, **2017**, 15, 9081-9094.

7. Wong, D. L.; **Zhang, A**.; Faponle, A. S.; de Visser, S. P.; Stillman, M. J. Glutathione binding to dirhodium tetraacetate: a spectroscopic, mass spectral and computational study of an anti-tumour compound. *Metallomics*, **2017**, 9, 501-516.

8. Yamamoto, S.; **Zhang, A**.; Stillman, M. J.; Kobayashi, N.; Kimura, M. Low-symmetry Ω-shaped zinc phthalocyanine sensitizers having panchromatic light-harvesting property for dye-sensitized solar cells. *Chem. Eur. J.*, **2016**, 22 (52), 18760-18768.

Oral Presentations:

1. **Zhang, A.**; Stillman, M. J. Computational and spectroscopic studies toward design of chlorophyll derivatives for photodynamic therapy. The 6th International Symposium on Metallomics (Metallomics 2017), Vienna, Austria, August 14-17, 2017.

2. Polgar, A.M.; Khadka, C. B.; Azizpoor Fard, M.; Cadogan, C.; **Zhang, A.**; Stillman, M. J.; Weigend, F.; Corrigan, J. F. Gold(I) Trimethylsilylchalcogenolate precursors to luminescent mixed coinage metal-chalcogenide clusters. 100th Canadian Chemistry Conference and Exhibition (CSC 2017), Toronto, May 28-June 1, 2017.

3. **Zhang, A.**; Stillman, M. J. Chlorophyll-like compounds for dye-sensitized solar cells. 6th Georgian Bay International Conference on Bioinorganic Chemistry (CanBIC-6), Parry Sound, Ontario, Canada, May 23-27, 2017.

Poster Presentations:

1. **Zhang, A.**; Stillman, M. J. Design concepts for enhanced efficiency of porphyrin dyes for dye-sensitized solar cells using MCD and DFT methods. International Conference on Porphyrins and Phthalocyanines (ICPP-10), Munich, Germany, July 1-6, 2018.

2. **Zhang, A.**; Yamamoto, S.; Kobayashi, N.; Kimura M.; Stillman, M. J. Design of porphyrin dyes using computational and spectroscopic methods for dye-sensitized solar cells. South African Chemical Institute Inorganic Chemistry Conference, Hermanus, Western Cape, South Africa, June 25-29, 2017.

3. **Zhang, A.**; Yamamoto, S.; Kobayashi, N.; Kimura, M.; Stillman, M. J. Design of porphyrin dyes using computational and spectroscopic methods for dye-sensitized solar cells. Fallona Family Interdisciplinary Showcase, The University of Western Ontario, London, Ontario, Canada, January 16, 2017.

4. **Zhang, A.**; Stillman, M. J. Computational and spectroscopic studies in the design of novel porphyrins for solar cell applications. International Conference on Porphyrins and Phthalocyanines (ICPP), Nanjing, China, July 3-8, 2016.

5. **Zhang, A.**; Stillman, M. J. Computational and spectroscopic studies in the design of novel porphyrins for solar cell applications. Graduate Student Symposium, Amherst, United States, May 16, 2016.

6. **Zhang, A.**; Stillman, M. J. Computational and spectroscopic studies in the design of novel porphyrins for solar cell applications. Symposium Phthalocyanines, Universidad Miguel Hernandez, Elche, Spain, January 27 and 28, 2016.

Related Experience:

CanBIC Local Organizing Committee, 2017
Programme Editor, Symposia Scheduling